Quantitative ultrastructural localization of voltage-gated calcium channel subunits in the mouse brain

Laxmi Kumar Parajuli

DOCTOR OF PHILOSOPHY

Department of Physiological Sciences
School of Life Science
The Graduate University for Advanced Studies

2012

Table of Contents

Localization of α1G subunit of T-type calcium channel in the mouse thalamus

Localization of α1E subunit of R-type calcium channel in the mouse brain

Acknowledgements

Summary

Multiple aspects of neuronal signaling in the brain are largely determined by the precise localization of ion channels in the neuronal plasma membrane. There are numerous ion channels in the brain, each serving distinct roles. In neuronal cells, Ca^{2+} influx through voltage–gated calcium channels (VGCC) are responsible for triggering plethora of subcellular responses such as exocytosis, plasticity, gene transcription etc. Despite these crucial roles, our fundamental understanding of the precise ultrastructural localization of VGCC lags behind that of other ion channels. Therefore, in order to obtain a more thorough understanding of the function(s) of VGCC in individual neurons and neuronal connections, it is important to know its precise localization in the brain.

To gain insight into subcellular distribution of VGCC, a number of studies have used techniques such as *in situ* hybridization, electrophysiological recordings and optical imaging. However, the technical limitations of these methods cannot provide a straightforward answer to the precise subcellular localization of VGCC. An obvious solution to this problem is to study VGCC localization at electron microscope (EM) level by means of subunit specific VGCC antibodies.

Appreciating the usefulness of EM techniques in revealing the neuronal distribution of VGCC, I have been using preembedding immunogold labeling technique in combination with serial section EM to study VGCC localization in the mouse and rat brain. To this end, I have studied the subcellular distribution of the α1G subunit of T-type VGCC (Parajuli et al., J Comp Neurol. 4362-4374; 2010), R-type VGCC (Parajuli et al., J Neurosci 32: 13555-13567), $Ca_v1.2$ VGCC (ongoing) and Beta subunits of VGCC (ongoing). In addition, I have also revealed the differential distribution of hyperpolarization cyclic nucleotide activated channel subunit 2 and 4 (HCN2 and HCN4) and their colocalization with α1G subunit of T-type VGCC in the thalamus (Parajuli et al., manuscript in preparation). This thesis will focus on the localization of $Ca_v2.3$ subunit of R-type calcium channel and $Ca_v3.1$ subunit of T-type calcium channel in the mouse brain. The results from other VGCC subunits will be reported elsewhere after completion of respective studies.

The T-type calcium channel localization (TTCC) study (Parajuli et al., J Comp Neurol. 4362-4374; 2010) was the first to give a definitive picture on the localization of

α1G subunit of TTCC. Previous electrophysiological and computational studies have suggested that in order to achieve appropriate thalamic oscillations TTCC must be non-uniformly distributed along the somatodendritic axis of thalamic neurons. However, by extensive 3D reconstruction of immunogold labeled dendrites and somata, I revealed that TTCC are uniformly distributed along the somatodendritic compartments of thalamic neurons. This immediately provokes an idea that non-uniform distribution of TTCC may not be a prerequisite for achieving thalamic oscillations.

I have made following observations regarding the localization of $Ca_v2.3$ subunit of R-type calcium channel (RTCC) in the brain.

1. RTCCs are expressed ubiquitously in the brain with higher levels in the hippocampus, striatum, amygdala, cortex, interpeduncular nucleus than other regions.

2. RTCCs are expressed predominantly presynaptic in the interpeduncular nucleus but predominantly postsynaptic in other regions.

3. RTCCs found in dendritic shafts and spines showed a higher density compared to somata in CA1 of the hippocampus.

4. Individual spine heads of the CA1 of the hippocampus contained 0 - 16 $Ca_v2.3$ particles in adult mouse and 0 – 19 $Ca_v2.3$ particles in postnatal day 20 rat, which is consistent with the number of RTCCs reported previously (Sabatini and Svoboda, 2000).

5. The number of RTCCs in the CA1 of the hippocampus spine is positively correlated to the spine head volume.

6. The number of RTCCs is highly variable among individual spines in the CA1 of the hippocampus.

7. The average density of RTCCs in spine has no correlation to the density in the parent dendrite in the CA1 of the hippocampus.

On a technical note, most of the immunogold quantification data found in the literature is obtained from single section analysis of ultrathin sections. This method has several technical pitfalls and introduces a large quantification bias. However, in my study, I partially reconstruct a neuron and perform immunogold quantification in the given reconstructed profile. This method is rather laborious and time consuming, but the quantification results are more reliable than that obtained from single section study.

In summary, my study provides detailed insight and fundamental knowledge of VGCC localization in the neurons.

General introduction

Background

      The biological significance of Ca^{2+} was first realized by Sydney Ringer in 1883 when he noticed that an isolated frog heart muscles can only maintain its contraction if Ca^{2+} is present in the bathing solution. About half a century later, Heilbrunn and Wiercinski in 1947 showed that the injection of Ca^{2+}, but not Mg^{2+}, Na^+ or K^+, into isolated frog muscle fibers resulted in muscle contraction. Despite these landmark observations, the physiological importance of Ca^{2+} was largely overlooked for a long time and received little attention as compared to Na^+. However, following the discovery by Katz and Miledi in 1965 that Ca^{2+} is required for neurotransmission, the interest in Ca^{2+} dramatically increased. Since then, Ca^{2+} continues to be the forefront of neuroscience research.

Neuronal Ca^{2+} conduits

      Cytoplasmic Ca^{2+} elevation can be brought about by plasma membrane calcium conduits or by calcium release through internal stores via calcium release channels such as inositol trisphosphate receptor (IP3) and ryanodine receptors. Based on the mode of activation, the plasma membrane calcium conduits can be classified as voltage-gated and neurotransmitter-gated. Voltage-gated calcium channels (VGCC), Hyperpolarization-activated cyclic nucleotide-gated (HCN) channels, and some members of transient receptor potential (TRP) channels are typical examples of voltage-gated plasma membrane calcium conduits. Glutamate receptors, nicotinic acetylcholine receptors and serotonin receptors are representative members of the ligand gated plasma membrane calcium conduits in the brain. Among all these calcium conduits, VGCC has attracted special attention as the calcium flux through VGCC mediates crucial neuronal functions such as neurotransmitter release and gene transcription.

Voltage-gated calcium channels (VGCC)

Structure of VGCC

      VGCC are heteromultimers composed of the pore forming α subunit of about 200-250 kDa, α2δ dimer complex of about 170 kDa, intracellular β subunit of about 55

kDa, and transmembrane γ subunit of about 30 kDa. The α2δ, β and γ subunit are termed as the auxiliary subunit as they modulate the biophysical properties of VGCC and govern the trafficking of the pore forming α subunit to the neuronal plasma membrane.

The α subunit, a protein of about 2000 amino acids, contains the channel pore, the voltage-sensor machinery and the binding sites for all known VDCC agonists and antagonists. It has four repeated homologous, highly hydrophobic, domains each containing six putative transmembrane spanning helices (S1-S6). The fourth helices (S4) of each domain are thought to act as a voltage sensor. The voltage sensor contains positively charged lysine and arginine residues at every third position. Voltage fluctuation causes movement of the voltage sensor causing the opening and closing of VGCC, due to its conformational change. The hydrophobic loop between the fifth and six helices (S5-S6) is thought to form the channel pore. Glutamate residues in the pore region are thought to result in the selectivity of VDCC to calcium ions. The α subunit also contains different putative sites for phosphorylation, and interaction of proteins such as G-protein or VDCC beta subunit etc.

The α2δ subunit, a protein of 1106 amino acid, is a disulfide linked complexes of extracellular, glycosylated α2 and a single transmembrane δ subunit. Although α2 were initially thought to contain transmembrane segments, the hydropathy analysis of primary amino acid structure has casted doubt and uncertainty. Interestingly, the δ subunit is encoded by the 3' end coding sequence of the same gene encoding α2 proteins. The α2δ complex, transcribed and translated from the same gene, is postranslationally cleaved into mature α2 and δ subunits at alanine 934 residue of the α2δ precursor protein. Amino acid residues 935-1106 encode the disulfide-linked δ subunit.

The β subunits are cytoplasmic proteins which lack the putative transmembrane segments and display four major alpha helices. Based on the sequence alignment of the four beta subunits (β1-β4), five amino acid sequence similarity domains are reported. The second domain contains a 30 amino acid region known as the beta interacting domain (BID). The BID is responsible for anchoring β subunits to an 18 amino acid region, known as alpha interacting domain (AID), present on the I-II loop of the high threshold α1 subunits.

The γ subunit is a hydrophobic, transmembrane protein containing several putative glycosylation sites.

Nomenclature of VGCC

Ten different genes encoding VGCC α1 subunits have been identified in mammals so far. They were often named differently by different scientists until 1994 when the first unified nomenclature proposed to name α1S for the skeletal muscle calcium channel and α1A-α1E for α1 subunits cloned subsequently. The four α1 subunits that have been identified since then have been named α1F through α1I. However, it did not take long to realize that this classification is arbitrary and fails to reveal the structure function relationship of α1 subunits. For example, α1S, α1C, α1D and α1F subunits have high sequence similarity and each subunit mediates L-type current. Despite that, these four subunits were not included in the same family. Therefore, since 2000, a new nomenclature has been adopted. According to this, the α subunits mediating the same calcium current types and displaying high sequence similarity of their amino acid residues are grouped in the same family. The α subunits mediating L-type current are included in Ca_v1 family, P/Q, N and R-type current in Ca_v2 family and T-type current in Ca_v3 family. Moreover, Subunits in a family show a significant sequence similarity (about 80%) in the amino acid residues. In contrast, subunits outside of the family display rather low sequence similarity (50% between Ca_v1 and Ca_v2 and 30% between Ca_v3 and Ca_v1 or Ca_v2). Consequently, the sequence analysis suggests that Ca_v1 and Ca_v2 families are phylogenetically closer to each other than Ca_v3 subunits.

Biophysical properties of VGCC

The amplitude, concentration and time course of the calcium transients in the plasmalemmal space surrounding the channel pore are largely determined by the biophysical properties of the channel. Thus, to put an ultrastructural data into a functional context, it is necessary to understand the biophysical properties of each of the VDCC α1 subunits. Each VDCC α subunit exhibits different biophysical properties that resembles closely within the subunits in the same family. The major biophysical and pharmacological properties of each of types of VGCC are tabulated below.

	L-type	P/Q-type	N-type	R-type	T-type
$\alpha 1$ subunit	$Ca_v1.1$, $Ca_v1.2$, $Ca_v1.3$, $Ca_v1.4$	$Ca_v2.1$	$Ca_v2.2$	$Ca_v2.3$	$Ca_v3.1$ $Ca_v3.2$ $Ca_v3.3$
Classification	HVA	HVA	HVA	HVA[1]	LVA
Conductance	20-25 pS in 110 mM Ba^{2+} (DRG)	9-19 pS in 100 mM Ba^{2+} (DRG)	13 pS in 110 mM Ba^{2+} (DRG)	15-20 pS in 90 mM Ba^{2+} (cerebellar granule cells)	5-9 pS in 100 mM Ba^{2+} (chick DRG)
Activation (τ_a)	1 ms at +10 mV	2.2 ms at +10 mV	2.8 ms at +20 mV	2.1 ms at -10 mV	1 ms at -10 mV
Inactivation (τ_h)	1100 ms at -20 mV	690 ms at +10 mV	112 ms at +20 mV	100 ms at -10 mV	11 ms at -10 mV
Blockers	verapamil	ω-agatoxin IVA	ω-conotoxin GVIA	SNX-482	Mibefradil

HVA: high-voltage-activated; LVA: low-voltage-activated; DRG: dorsal root ganglion

[1]The activation threshold voltage of RTCC lies between that of HVA and LVA classes of VGCC. Therefore, RTCC is classified by some researchers as an intermediate-voltage-activated calcium channel.

.

Chapter 1: Subcellular distribution of α1G subunit of T-type calcium channel in the mouse dorsal lateral geniculate nucleus

ABSTRACT

T-type calcium channels play a pivotal role in regulating neural membrane excitability. However, the precise subcellular distributions of T-type channel subunits are not well understood. Here, I investigated the subcellular distribution of the α1G subunit of the calcium channel which is expressed highly in the mouse dorsal lateral geniculate nucleus (dLGN). Light microscopic analysis demonstrated that dLGN exhibits intense immunoperoxidase reactivity for the α1G subunit. Electron microscopic observation showed that the labeling was present in both the relay cells and interneurons and was found in the somatodendritic, but not axonal, domains of these cells. Most of the immunogold particles for the α1G subunit were either associated with the plasma membrane or the intracellular membranes. Reconstruction analysis of serial electron microscopic images revealed that the intensity of the intracellular labeling exhibited gradient such that the labeling density was the highest in the proximal dendrite and progressively decreased towards the distal dendrite. In contrast, the plasma membrane associated particles were distributed with a uniform density over the somatodendritic surface of dLGN cells. The labeling density in the relay cell plasma membrane was about three-fold higher than that of the interneurons. These results provide ultrastructural evidence for cell-type specific expression levels and for uniform expression density of the α1G subunit over the plasma membrane of dLGN cells.

INTRODUCTION

The opening of voltage-gated calcium channels (VGCC) leads to transient increases in intracellular Ca^{2+}. The location of calcium influx is strictly regulated to control the activation of calcium-dependent processes, such as neurotransmitter release, neuronal excitation, and regulation of gene expression. Biophysical and pharmacological studies have led to the identification of high-voltage-activated (HVA) calcium channels (L-, N-, P/Q-, and R-types) and a low-voltage-activated (LVA) T-type calcium channel (for reviews, see Jones, 1998; Catterall, 2000). Members of the HVA calcium channels require a larger membrane depolarization for their opening than the LVA T-type calcium channel. The latter is mostly inactivated at neuronal resting potential, thus, a brief hyperpolarization is required for the channel to deinactivate prior to activation (Jansen et al., 1984; Perez-Reyes, 2003). Among the three different genes encoding T-type VGCC α1 subunits (Cav3.1/α1G, Cav3.2/α1H, and Cav3.3/α1I), the α1G subunit is highly expressed in the thalamus (Talley et al., 1999). It has been shown to play a prominent role in the generation of low-threshold spikes leading to thalamic burst firing and slow-wave sleep oscillations (Steriade et al., 1988; Huguenard, 1996; Kim et al., 2001; Lee et al., 2004; Song et al., 2004; Anderson et al., 2005).

Neuronal excitability is thought to be dependent on the precise spatial distribution of voltage-gated ion channels. In the thalamus, although previous studies have suggested postsynaptic (dendrites and soma) expression of the α1G channel subunit, their relative distribution along the somatodendritic axis of the thalamic neurons has not yet been fully elucidated and is a matter of debate. An earlier electrophysiological and computational modeling study suggested an enrichment of this subunit in the distal part of the dendrite (Destexhe et al., 1998) whereas others have suggested its predominant somatic and proximal dendritic localization (Munsch et al., 1997; Zhou et al., 1997; Williams and Stuart, 2000; Zhuravleva et al., 2001; Rhodes and Llinas, 2005). In a recent computational modeling study, it was suggested that the appropriate thalamic oscillation can be achieved even if the T-type calcium channels are distributed uniformly throughout the somatodendritic arbor (Zomorrodi et al., 2008). Although informative, the data

obtained from these previous studies remain largely speculative due to the lack of a selective T-type calcium channel blocker and unequivocal criterias to define the T-type current. Furthermore, these studies are technically constrained due to the seemingly challenging limitation of resolving the calcium signals from the fine-caliber distal dendrites. Therefore, a precise and quantitative subcellular localization of this channel has been the subject of considerable interest.

Immunoelectron microscopy is an indispensable method for studying the ultrastructural localization of channel molecules. However, to date our potential understanding of the α1G distribution has been hampered by the lack of specific antibodies against this subunit applicable for immunoelectron microscopy. In this study, I used a newly developed antibody specific for the mouse α1G subunit and employed high-resolution immunoelectron microscopy to reveal the relative distribution of the α1G subunit in the somatodendritic axis of the dorsal lateral geniculate nucleus (dLGN) neurons. My results demonstrate a uniform distribution of the α1G subunit over the somatodendritic plasma membrane of the dLGN neurons.

MATERIALS AND METHODS

Animals

Ten eight-week-old male wild-type (WT) mice (C57BL/6Cr Slc) and four eight-week-old α1G-deficient mice (Kim et al., 2001) were used for this study. The animals were raised in a normal light dark cycle with free access to food and water. Efforts were made to minimize the number of animals and pain and suffering of the animals used. All experimental procedures performed on the animals were carried out in accordance with the guidelines of the animal care and use committee of the National Institute for Physiological Sciences (Okazaki, Japan) and approved by the committee.

Fixation

For light microscopic observation, mice were deeply anaesthetized with sodium pentobarbital (*ip*, 50 mg/kg body weight) and perfused with 25 mM phosphate buffered saline (PBS) for 1 min followed by a fixative containing 4% paraformaldehyde and 15% saturated picric acid in 0.1 M phosphate buffer (PB, pH 7.4). For electron microscopic observation, anaesthetized mice were fixed with the same fixative solution containing 0.1% glutaraldehyde (Polysciences, Warrington, PA). After fixation, 50 μm coronal sections were cut on a slicer (Leica, VT-1000, Austria). The sections were washed twice in PB and then processed for immunolabeling.

Antibody characterization

Primary antibodies used in this study are listed in Table 1. A guinea pig polyclonal antibody for the α1G subunit of the T-type calcium channel was raised against the C-terminal sequence of mouse $Ca_v3.1$. The specificity of the anti-α1G antibody has been previously confirmed by immunohistochemical analysis (Hildebrand et al., 2009). The previous study demonstrated that the intense immunofluorescent signal observed in the cerebellum and thalamus of the WT mouse was absent in the brain sections from α1G knock-out (KO) mouse. In the present study, I further confirmed the specificity of the antibody. At both the light microscopic and electron microscopic levels, the strong

labeling observed in the thalamus of the WT mouse was abolished in the α1G KO mice (Fig. 1, Supporting Figs. 1 and 2), thereby providing evidence for the specificity of my immunolabeling. A mouse monoclonal antibody for glutamic acid decarboxylase (GAD; Chemicon, MAB351) used in this study has been shown to recognize the lower molecular weight isoform (65 kDa) of the two GAD isoforms identified in the brain (Chang and Gottlieb, 1988).

Immunohistochemistry for light microscopy

Fixation, labeling conditions, and antibody concentration were rigorously optimized during initial pilot experiments. Sections were blocked with 10% normal goat serum (NGS; Vector laboratories, Burlingame, CA) and 0.1% Triton X-100 in PBS for 1 h and then incubated overnight at 4^oC with the primary antibody against α1G (1 μg/ml) in PBS containing 2% NGS and 0.05% Triton X-100. After several washes in PBS, sections were incubated with a biotinylated goat anti-guinea pig IgG antibody (1:200; Vector laboratories, Burlingame, CA) diluted in 25 mM PBS containing 2% NGS and 0.05% Triton X-100 at room temperature for 1 h. The sections were washed with PBS and reacted with avidin-biotin peroxidase complex (1:100 ABC-Elite; Vector laboratories) diluted in PBS containing 0.1% Triton X-100 for 1 h at room temperature. After washing thrice in PBS, the sections were washed once in 50 mM Tris-HCl buffer (pH 7.6) and then incubated at room temperature in the buffer supplemented with 0.025% 3,3'- diamino benzidine tetrahydrochloride (DAB; Dojindo Lab., Kumamoto, Japan) and 0.003% hydrogen peroxide. Upon reaching the appropriate signal intensity, DAB reaction was terminated. Sections were then mounted on glass slides, dehydrated in graded alcohol, and covered with cover slips.

Electron microscopic immunoperoxidase labeling

Sections were cryoprotected in a solution containing 25% sucrose and 10% glycerol in 20 mM PB and freeze-thawed with liquid nitrogen. After several washes in 50 mM Tris-HCl buffered saline (TBS), the sections were blocked with 20% NGS in TBS

for 1 h and then processed similarly as described for light microscopic immunohistochemistry except that Triton X-100 was omitted in all the steps. After the development of immunoperoxidase reaction, sections were fixed with 1% OsO_4 for 40 min, stained with 1% uranyl acetate for 35 min, dehydrated, and flat-embedded in Durcupan resin (ACM Fluka, Sigma-Aldrich, Gillingham, Dorset, UK). Ultrathin sections of 70 nm thickness were prepared using an ultramicrotome (Ultracut T; Leica), post-stained briefly with lead citrate and observed under a transmission electron microscope (EM208S; Philips, Eindhoven, The Netherlands). Digital images were obtained using MegaView III CCD camera (Olympus-SIS GmbH, Germany) and processed with iTEM software (Olympus-SIS) and Photoshop (Adobe, San Jose, CA) for image analysis and preparation of figures, respectively.

Three-dimensional reconstructions of neuronal profiles were carried out with serial ultrathin sections using a Reconstruct software (Fiala, 2005).

Electron microscopic immunogold labeling

Sections were freeze-thawed as described above. After several washes in TBS, the sections were blocked with 5% acetylated bovine serum albumin (BSA-C; Aurion, Wageningen, The Netherlands) and 5% NGS in PBS for 1 h. The sections were then washed twice with PBS containing 0.2% BSA-C (PBS/BSA-C) and incubated overnight at $4^{o}C$ with the α1G antibody diluted at 1 μg/ml in PBS/BSA-C. After washing with PBS/BSA-C, sections were incubated overnight at $4^{o}C$ with 0.8-nm gold conjugated goat anti-guinea pig secondary antibody (1:100; Aurion) diluted in PBS/BSA-C. After several washes with PBS-BSA/C, the sections were further washed with enhancement conditioning solution (ECS; Aurion). The sections were then silver-intensified with the R-Gent SE-EM intensification kit (Aurion). After washing, the sections were fixed with 1% OsO_4, stained with uranyl acetate, dehydrated, and flat-embedded in Durcupan resin.

Double immunolabeling was performed using the guinea pig polyclonal antibody against α1G and the mouse monoclonal antibody against GAD. Sections were incubated in a mixture of the anti-α1G (1 μg/ml) and anti-GAD (1 μg/ml) antibodies. Thereafter,

they were incubated overnight with biotinylated anti-mouse (1:100; Vector laboratories) and gold-conjugated goat anti-guinea pig secondary antibodies (1:100; Aurion). Following silver intensification for α1G, peroxidase reaction for GAD was performed.

Immunogold quantification

Among various thalamic nuclei, this study particularly focused on the dLGN because its neural circuitry has been well characterized. Furthermore, the electrophysiological properties of neuronal cells in this nucleus have been extensively studied. In addition, as dLGN is the only thalamic nucleus containing both principal neurons and local circuit interneurons (Ohara et al., 1983; Paxinos, 1995; Arcelli et al., 1997), it also provides a unique possibility to compare α1G expressions between principal neurons and local circuit interneurons.

The subcellular distribution of α1G was analyzed from two WT mice for single labeling and one WT mouse for double labeling. In order to sample the profiles within the optimal penetration depth of the antibody, electron micrographs were obtained within 1-3 μm from the resin-tissue interface. To ascertain that a specific dendrite is immunolabeled, 20-30 serial ultrathin sections were collected on the same grid for quantification purposes.

In the single labeling experiment, the relay cells were distinguished from the interneurons based on their morphological criteria. Any dendritic profiles containing flattened and pleomorphic synaptic vesicles were identified as interneuron processes. Somatic profiles were identified as interneurons if they have a small somatic diameter with nuclear infoldings (Jones, 2007). When encountered, such processes were omitted from the quantification study performed from the single labeling experiment which focused only on the relay cell processes. However, it should be noted that the electron microscopic immunolabeling study makes use of a mild tissue fixation condition which hinders the optimal ultrastructural preservation. Thus, to investigate labeling in interneurons, GAD immunoreactivity was used as a marker for reliable distinction of interneurons from the relay cells in another separate set of experiments.

The retinogeniculate axon terminal was distinguished from the corticogeniculate axon terminal based on their morphological features. Large terminals containing round synaptic vesicles and pale mitochondria were identified as retinogeniculate terminals, whereas small terminals containing round synaptic vesicles and dark mitochondria were identified as corticogeniculate terminals (Lieberman and Webster, 1974).

Twenty-eight different dendritic segments and three different somatic segments were reconstructed from 20 to 25 serial ultrathin sections. The dendritic diameter of individual reconstructed profiles was measured as the widest transect of the narrowest dimension of the ovoid profile of the dendrite (Hanson and Smith, 2002). A dendritic diameter is an indirect measure of the distance from the soma since the minor diameter of a dendrite progressively decreases with increasing distance from the soma. Linear density of the gold particles in the plasma membrane was obtained by dividing the total number of plasma membrane-bound immunogold particles (see text for the criteria) by plasma membrane length of individual reconstructed dendrites. Dendritic surface area was calculated by multiplying the total plasma membrane length of each reconstructed dendrite by the section thickness (70 nm). The total number of plasma membrane-bound gold particles found in a reconstructed dendrite was divided by the dendritic surface area to obtain the labeling density of plasma membrane-bound particles in individual profiles. For calculating the density of internal membrane-bound particles, the total number of intracellular particles found in a profile was divided by the dendritic cross-sectional area.

Synaptic, perisynaptic and extrasynaptic areas were defined according to the method described by Barthó et al. (2004). Briefly, the synaptic area was calculated from synaptic lengths in a series of EM images and the section thickness (70 nm) as shown in the formula below.

$A_{syn} = [(l_{first}+l_{second}) + (l_{second}+l_{third}) + \ldots + (l_{last-1}+l_{last})] \times 0.07 / 2$,

where l_{first}, l_{second}, l_{third}, $\ldots l_{last}$ refer to the synaptic length of the first, second, third, … last section of the series containing the given synapse. Perisynaptic plasma membrane area, defined as an annulus surrounding a synapse by 200 nm in this study, was determined by an approximation of the area occupied by two rectangles on the top and bottom of the

synapse, two parallelograms on the sides of the synapse and four quarters of a cycle connecting the rectangles and the parallelograms. It can be formulated as:

$A_{perisyn} = (l_{first}*0.2) + (l_{last}*0.2) + [0.2*0.07*(n-1)*2] + (0.2^2 * 3.14)$, where n refers to the number of sections containing that synapse. Extrasynaptic areas were obtained after subtracting the synaptic and perisynaptic areas from the total surface area of the reconstructed dendrites. In order to compare labeling densities for α1G between perisynaptic and extrasynaptic areas, only dendrites in which synapses located within at least 3 sections (~ 210 nm) inside from the top and bottom edge of the reconstructed dendrite were used. Out of 28 reconstructed dendrites, this criterion was fulfilled by 6 dendrites. A total of 9 synapses were found in these 6 dendrites. Membrane-bound particles for α1G were divided into two groups as perisynaptic particles and extrasynaptic particles, and the labeling densities within these two membrane domains were calculated.

Statistical analysis

Statistical analysis was performed using SPSS (SPSS Inc., Chicago, IL). Shapiro-Wilk's W-test was applied for checking the normality of the data sets. The statistical significance between groups was analyzed by the two-tailed unpaired Student *t*-test and Mann-Whitney U-test for parametric and non-parametric analysis, respectively. One-way ANOVA was used for statistical comparison among multiple groups. Correlation analysis was performed using Spearman's rank order test. Statistical significance was defined as *P* < 0.05. The data in the text are expressed as mean ± SEM.

RESULTS

Distribution of α1G immunoreactivity in the thalamus

At the light microscopic level, immunolabeling for α1G revealed a specific pattern of α1G distribution in the thalamic nuclei. A majority of the thalamic nuclei exhibited a moderate to strong labeling for α1G (Fig. 1 and Supporting Fig. 1). A strong immunoreactivity was observed in the midline thalamic nuclei (e.g., paraventricular thalamic nucleus and reuniens nucleus), anterior thalamic nuclei (e.g., laterodorsal thalamic nucleus), medial thalamic nuclei (e.g., mediodorsal thalamic nucleus), and ventral motor nuclei (e.g., ventral lateral, ventral medial). Intralaminar nuclei such as the parafasicular nucleus had a moderate level of α1G immunoreactivity. In the epithalamus, the lateral habenula showed a strong immunoreactivity whereas the immunoreactivity in the medial habenula was weak. In the geniculate complex, dLGN and the magnocellular part of ventral LGN showed strong reactivity compared to the very weak immunoreactivity observed in the parvocellular part of ventral LGN. The ventrobasal nucleus, one of the major thalamic relay nuclei, also showed strong immunoreactivity for α1G. The dLGN, which is the visual first order relay nucleus, had a stronger immunoreactivity than its corresponding higher order counterpart nuclei, the lateral posterior nucleus. In contrast to the dLGN, the labeling in the thalamic reticular nucleus (TRN) which contains no relay cells was below the detection limit (Supporting Fig. 1). No immunoreactivity for α1G was detected in the white matter. The α1G labeling observed in the WT mice was completely abolished in the KO animals (Fig. 1, Supporting Figs. 1 and 2).

α1G immunoreactivity at electron microscopic level

The immunoperoxidase reaction was performed to determine the distribution of α1G immunoreactivity at the subcellular level. The peroxidase reaction end product was observed exclusively in dendrites and somata but not in axons and presynaptic terminals (Fig. 2A). Qualitatively, a large number of dendrites were positive for α1G. Peroxidase

labeling revealed that the dendrites postsynaptic to putative retinal as well as cortical terminals were both immunopositive.

Next, to reveal the precise location of the channels at a greater spatial resolution, immunogold labeling was performed. Immunogold particles for α1G were observed in small- and large-caliber dendrites as well as in the somata in close correspondence with the peroxidase labeling (Fig. 2B, C). The gold particles were localized intracellularly as well as in close proximity to the plasma membrane. Virtually no immunoparticles for α1G were observed in the slices obtained from the KO animal (Supporting Fig. 2).

Distribution of α1G immunogold particles in relation to membrane structures

To analyze the location of immunogold particles relative to the nearest membrane structures, the distance from the center of the individual gold particles to the middle of the nearest membrane structures were measured in one WT specimen. The measured distance for each gold particle was subjected to histogram analysis with a bin width of 5 nm and plotted against the frequency of profiles (Fig. 3). Although the distance distribution of the gold particles (n = 179) did not follow a Gaussian distribution ($P <$ 0.001, Shapiro-Wilk's W-test), the data plot revealed a single peak at 10-15 nm (mean = 16.6 ± 0.82 nm, median = 14.6 nm). This suggests membrane origin of those immunogolds.

Relative proportion of the plasma membrane- and intracellular membrane-bound immunogolds

To quantify the proportion of α1G present in the plasma versus intracellular membranes, all the immunoparticles were categorized either as plasma membrane- or internal membrane-bound. Based on the particle distribution histogram presented in Figure 3, about 95% of the immunoparticles were located within 42 nm (mean + 2 S.D.) from the membrane structures. Thus, particles located within 42 nm from the plasma membrane towards the cell interior were categorized as plasma membrane-bound particles and the rest of them as intracellular membrane-bound particles (Fig. 4). From a

total of 1284 immunogold particles analyzed, 118 particles were observed in the small-caliber (< 0.5 μm) distal dendrites (n = 9), of which 98 (83%) were plasma membrane-bound and 20 (17%) were internal membrane-bound. Of 143 particles observed in the medium-caliber (0.5 μm-1.0 μm) dendrites (n = 7), 94 (65.7%) were plasma membrane-bound and 49 (34.3%) were internal membrane-bound. In the large-caliber (> 1.0 μm) proximal dendrites (n = 12), 1023 particles were observed, of which 400 (39.1%) were plasma membrane-bound and 623 (60.9%) were internal membrane-bound. In total, 592 (46.1%) particles were found to be associated with the plasma membrane and the remaining 692 (53.9%) particles were associated with the internal membrane.

Densities of α1G immunogold particles over somatodendritic compartments

In recent years, a number of studies have shown that certain ion channels can be selectively targeted to specific membrane compartments. In dLGN, previous electrophysiological studies have suggested an uneven distribution of T-type calcium channels between the somata and the dendrites (Munsch et al., 1997; Zhou et al., 1997; Destexhe et al., 1998; Williams and Stuart, 2000; Zhuravleva et al., 2001; Rhodes et al., 2005). I therefore aimed to determine if indeed α1G shows such compartmentalized distribution in the somatodendritic domains of dLGN cells. In serial sections, the immunogold particles for α1G were observed both in the small- and large-caliber dendrites (Fig. 5A - H). No correlation between the dendritic diameter and the immunogold linear density was detected (Fig. 6A, r = - 0.209, *P* = 0.286, n = 28). Similarly there was no significant difference in the immunogold density between the somatic (0.194 ± 0.004 particle/μm, n = 3) and dendritic (0.182 ± 0.012 particle/μm, n = 28) compartments (*P* = 0.640, Mann-Whitney U-test). Mean linear density values corresponded to 2.77 particle/μm^2 (range, 2.71-2.88) and 2.60 particle/μm^2 (range, 1.01-4.71) in the somatic and dendritic compartments, respectively. It is also important to mention that there was a high variability in the labeling density even among the dendrites of similar dendritic diameters (Fig. 6A). Similar proximodistal distribution and labeling patterns were obtained from another WT animal in which 30 dendritic segments and 6

somatic segments were reconstructed from 28-30 serial ultrathin sections collected on a single grid (data not shown).

Since a large fraction of immunoparticles were found to be associated with the intracellular membranes, I quantified and compared the intracellular labeling density in relation to the dendritic diameter. When the proportion of intracellular membrane-bound immunogold particles was examined in relation to the dendritic diameter, a weak positive correlation was observed (for related information, see Fig. 4, r = 0.909, P < 0.001, n = 28). Moreover, the density of intracellular membrane-bound particles also increased with dendritic diameter (Fig. 6B, r = 0.559, P = 0.002, n = 28).

No accumulation of α1G immunogolds nearby synaptic junctions

At the electron microscopic level, α1A and α1G subunits of calcium channels have been shown to localize mainly in the dendritic spines in the cerebellum, suggesting the role of these channels in synaptic events (Kulik et al., 2004; Hildebrand et al., 2009). In the present study, even though in some cases the gold particles for α1G were observed near to the synapse, no clear preference of the gold particles to the synaptic, perisynaptic, or extrasynaptic sites could be established in the serially reconstructed dendrites (Fig. 5I-L). Rather, the immunoparticles were found to be diffusely scattered all over the dendritic plasma membranes.

This qualitative observation was further supported by the results obtained from the quantitative analysis of the immunogold density in relation to the perisynaptic (an annulus surrounding a synapse by 200 nm) and extrasynaptic areas. The average immunogold densities were 3.34 ± 0.96 (range 0.00-7.25, n = 9) particles/μm^2 and 3.13 ± 0.26 (range 1.76-3.89, n = 6) particles/μm^2 in the perisynaptic and extrasynaptic areas, respectively, and were not significantly different (P = 0.841, unpaired Student t-test).

α1G labeling in interneurons

Despite the wealth of data about the expression of T-type calcium channels in principal neurons, little is known about their expression in interneurons. With this incentive, double labeling for GAD and α1G was performed to analyze α1G distribution in the GABAergic interneuron. Figure 7 shows two consecutive serial sections with a GAD-positive interneuron dendrite (i) and a relay cell dendrite (r) located adjacent to each other. The relay cell dendrite was well labeled in comparison to the interneuron dendrite. Serial reconstruction analysis (10-15 sections) revealed a linear density of 0.063 ± 0.015 particle/μm in the dendritic (n = 19) and 0.026 ± 0.022 particle/μm in the somatic compartments (n = 3) of the interneuron, with no significant difference ($P = 0.356$, Mann-Whitney U-test). GAD negative dendritic profiles had a linear density of 0.206 ± 0.021 in the dendritic (n = 22) and 0.244 ± 0.037 particle/μm in the somatic (n = 3) compartments. These density values for the relay cell were similar to that obtained from the single labeling experiment. The quantitative analysis revealed 3.3-fold higher labeling density in the plasma membrane of the relay cell dendrite when compared to the interneuron dendrite ($P < 0.001$, Mann-Whitney U-test). Moreover, this difference was as high as 9.4-fold in the case of labeling densities between the somatic compartments of these two cell populations ($P < 0.001$, Mann-Whitney U-test). This suggests that despite the presence of α1G channels in interneurons, they were expressed at much lower level when compared to those in the relay cells.

I also examined the relationship between the α1G expression density in the interneurons and their dendritic diameter. The average linear densities of immunogold particles associated with interneuron dendrites of different diameters were 0.054 ± 0.048 particle/μm, 0.064 ± 0.034 particle/μm, and 0.086 ± 0.034 particle/μm in the small-caliber (< 0.5 μm), medium-caliber (0.5 μm-1.0 μm) and large-caliber (> 1.0 μm) dendrites, respectively (Fig. 8). There were no significant differences in the relative abundance of the labeling among these compartments (one-way ANOVA, $F_{2,16} = 0.260$, $P = 0.775$). Again, the plasma membrane of the relay cells showed a uniform labeling density among different dendritic compartments in the double labeling experiment (one-

way ANOVA, $F_{2,19} = 0.016$, $P = 0.984$). These observations further corroborate the uniform proximodistal distribution of α1G channels in the plasma membrane of dLGN cells.

DISCUSSION

The spontaneous rhythmic activities of thalamic relay cells crucially depend on the α1G subunit of T-type calcium channel. α1G KO mouse shows a complete loss of relay cell burst response (Kim et al., 2001). Using a highly specific antibody against α1G, this study revealed the detailed distribution of the α1G in the dendritic arbor in the dLGN neurons. The results suggest that α1G molecules are distributed with a uniform density over the somatodendritic plasma membrane compartments of the mouse dLGN cells.

Regional distribution of α1G in the thalamus

This study found immunoreactivity for the α1G subunit in the majority of the thalamic nuclei besides the thalamic reticular nucleus. The regional distribution of α1G immunoreactivity in the thalamus is in agreement with the previously reported *in situ* hybridization studies (Zhang et al., 2002; Lein et al., 2007; Ernst et al., 2009) and an electrophysiological study (Chemin et al., 2002) which suggested the predominant expression of α1G in relay cells. However, my study differs from that of Mckay et al. (2006) and Kovács et al. (2009). In these two studies, strong immunostaining in the TRN of rats and cats was observed. However, there remains uncertainty about the specificity of their immunolabeling as immunostaining data in KO mice was not presented in their study. Furthermore, my data can be easily reconciled with the previous *in situ* hybridization study which had no detectable expression of α1G in the rat TRN (Talley et al., 1999).

Possible functional significance of the uniform density of α1G over somatodendritic plasma membrane of dLGN

The dendrites of principal relay neurons receive glutamatergic afferents in a compartmentalized manner with the sensory input generally contacting the proximal part of the relay cell dendrite and the cortical input preferentially contacting the distal part (Murphy and Sillito, 1987; Robson, 1993; Sherman and Guillery, 1998). Thalamic reticular axons make contacts throughout the dendritic arbor (Liu et al., 1995). In line with these morphological observations, the uniform distribution of α1G along the dendritic plasma membrane suggests an efficient means of achieving rebound bursting during the slow-wave sleep. The GABA release from TRN axons can effectively de-inactivate dendritically localized T-type calcium channels and enables their activation with incoming glutamatergic signals (Contreras et al., 1993; Zhan et al., 2000). Thus, the expression of α1G in both the proximal and distal dendrites will be beneficial for the amplification and faithful propagation of signals both at the cortical and sensory input sites.

The study revealed that the density of the plasma membrane particles is uniform throughout the somatodendritic compartments of the dLGN relay neuron (Figs. 6A, 8). However, the ratios of surface area against volume change along the somatodendritic compartments; the soma has the smallest and the distal dendrite has the largest ratio. Taking this into consideration, the different ratios are likely to result in a proportionally larger effect of T-type calcium channels in the distal dendrite when compared with the proximal dendrite. It has been suggested that the EPSP generated in the distal part will be attenuated on the way to the soma (Bloomfield et al., 1987). Therefore, placing a higher number of calcium channels in the distal dendrite may also be important to counteract the cable filtering effect.

Comparison with other studies

In my study, I found a uniform density of α1G in the soma and different membrane compartments of the dendrites. However, previous studies suggest that T-type calcium channels are distributed in a compartmentalized manner. Based on electrophysiological recording and computational modeling, Destexhe et al. (1998) have inferred a higher density of T-type calcium channel in the dendrites when compared with cell somata. By electrophysiological recording, they estimated that the density in the soma was 4.5-7.6 times smaller than in the dendrites (density in the dendrites: 8-14 $pS/\mu m^2$ (= 1.07-1.87 channels/μm^2; single channel conductance taken as 7.5pS, Perez-Reyes et al., 1998)). Similarly, using their estimated density in soma and dendrites, they could also reproduce their recorded traces in the computational modeling study. However, it should be noted that the density values estimated by Destexhe et al. (1998) are an underrepresentation of the actual *in situ* density of T-type calcium channel. Even by applying pre-embedding immunogold labeling, a method considered to have low detection sensitivity for their targets, I could obtain an average labeling density of 2.60 particles/μm^2 for α1G in the relay cell dendrites. Thus, as a result of underrepresentation, the validity of Destexhe et al.'s conclusion remains ambiguous.

To complicate the issue further, an electrophysiological study by Williams and Stuart (2000) reported a higher density of T-type calcium channel in the proximal dendrite and soma of dLGN neurons, a conclusion which is in sharp contrast to mine as well as Destexhe et al.'s study. However, due to the technical difficulty in patching from very fine distal dendrites, these authors limited their study to the proximal 60 μm length of the dendritic arbor. Since thalamic dendrites can extend as far as roughly 200 μm (Ohara and Havton, 1994), William and Stuart's study in effect investigated the channel distribution within a short dendritic segment.

A recent computational study by Zomorrodi et al. (2008) has suggested that the thalamic oscillations can be generated under uniform somatodendritic distribution of T-type channels. My experimental data together with the computational study raises the

possibility that the non-uniform distribution of the T-type calcium channel may not be a prerequisite for thalamic bursting.

Intracellular T-type calcium channel

In this study, I found a large pool of intracellularly localized immunogold particles. This is somewhat unexpected for transmembrane proteins such as ion channel. At present, the specific roles of these intracellularly localized T-type channels remain unclear. However, it is possible that the large amount of intracellular labeling observed in my experiment represents the newly synthesized α1G translocating from the site of synthesis to the plasma membrane. Some other cytoplasmic labeling may also represent the channels undergoing internalization and sequestration from the site of action. Importantly, the significant amount of intracellular labeling may also suggest an inefficient trafficking of α1G to the plasma membrane. My data is consistent with the ongoing notion that the T-type calcium channels α subunit lack the alpha interacting domain (AID), a motif necessary for its binding to β subunits and subsequent trafficking of the α-β complex towards the plasma membrane.

Variability in T-type calcium channel labeling density

My study showed variability in the labeling density of the membrane-bound α1G even within the dendrites of similar diameters (Fig. 6A). This is consistent with the results of dendritic patch attached recordings in the dLGN, where the amplitude of the T-type calcium current was variable among different dendrites located at the same distance from the soma (Williams and Stuart, 2000). Similarly, another calcium imaging experiment also revealed a high variability in the magnitude of calcium transients among different dendrites in the thalamic paraventricular nucleus (Richter et al., 2006). The variability in the T-type calcium channel density suggests that thalamic dendrites may differ in terms of their oscillatory activities.

α1G expression in the dLGN interneurons

Due to the very small magnitude of rebound burst observed in interneurons, earlier studies suggested the lack of T-type calcium channels in these cells (McCormick and Pape, 1988). However, in later studies it was shown that interneurons can generate burst firing in response to the injected current (Pape and McCormick, 1995; Munsch et al., 1997; Zhu et al., 1999; Broicher et al., 2007). The lack of burst firing in the interneurons in the earlier study was later reconciled to be due to the presence of A-type potassium current which has an antagonistic effect in terms of net membrane current, thereby preventing the generation of low-threshold spikes (Pape et al., 1994). Here, I provide ultrastructural evidence for the presence of α1G in dLGN interneurons.

Some interneuron dendrites were unlabeled throughout the serial section observed. The inclusion of such profiles resulted in large error bars as shown in Figure 8. The fact that I did not observe immunolabeling in some of the interneurons may suggest that there are different populations of interneurons in the dLGN and α1G may be expressed by interneuron subpopulation/s. There is indeed anatomical evidence suggesting the presence of at least two populations of interneurons in the dLGN (Gabbott and Bacon, 1994).

Technical consideration of my study

In contrast to this study which focused on 8-week-old adult mice, the electrophysiological studies are usually performed in young animals where the visual system is not fully mature and is still in the developmental stage. In view of the fact that the somatodendritic T-type calcium transients may vary during development (Pirchio et al., 1990; Yunker et al., 2003), the subcellular redistribution of α1G in adult mice compared to the postnatal age mice cannot be excluded. Comparing the present results with electrophysiological data obtained from the age-matched tissues would be informative and helpful in understanding the mechanisms underlying bursting activity in the adult dLGN neurons.

This study did not reveal any obvious preference of α1G molecules for the synaptic sites. However, this finding should be interpreted with caution as most of the antibodies fail to detect target antigens located at the postsynaptic density (for review, see Masugi-Tokita and Shigemoto, 2007). Along the same line, it also remains possible that the immunonegative interneuron profiles might express α1G at a low level but my method may have been insensitive to detect those.

The quantification of the channel proteins detected by the immunogold method may not necessarily correlate with the expression density of the functional channel. Calcium channels may either be in a phosphorylated or non-phosphorylated state (for review, see Catterall, 2000) and the phosphorylation of α1G molecules potentiates T-type calcium current amplitude in the thalamocortical neurons (Leresche et al., 2004; Park et al., 2006). Thus, even if the channels are distributed uniformly *in situ*, the electrophysiological responsiveness of these channels might differ at various neuronal compartments depending on their phosphorylation states (Zomorrodi et al., 2008).

In conclusion, the present results revealed that the α1G subunit of T-type calcium channels are uniformly distributed in the somatodendritic plasma membrane compartments of dLGN neurons. Further studies on the relative spatial localization of α1G to other ionic channels important for thalamic bursting might substantiate our current understanding of rhythmic activities of thalamic neurons.

References

Anderson MP, Mochizuki T, Xie J, Fischler W, Manger JP, Talley EM, Scammell TE , Tonegawa S. 2005. Thalamic Cav3.1 T-type Ca^{2+} channel plays a crucial role in stabilizing sleep. Proc Natl Acad Sci USA 102:1743–1748.

Arcelli P, Frassoni C, Regondi MC, Biasi SD, Spreafico R. 1997. GABAergic Neurons in mammalian thalamus: a marker of thalamic complexity. Brain Res Bull 42:27-37.

Barthó P, Payne JA, Freund TF, Acsády L. 2004. Differential distribution of the KCl cotransporter KCC2 in thalamic relay and reticular nuclei. Eur J Neurosci 20:965-975.

Bloomfield SA, Hamos JE, Sherman SM. 1987. Passive cable properties and morphological correlates of neurones in the lateral geniculate nucleus of the cat. J Physiol (Lond) 383:653-692.

Broicher T, Kanyshkova T, Landgraf P, Rankovic V, Meuth P, Meuth SG, Pape HC, Budde T. 2007. Specific expression of low-voltage-activated calcium channel isoforms and splice variants in thalamic local circuit interneurons. Mol Cell Neurosci 36:132-145.

Catterall WA. 2000. Structure and regulation of voltage-gated Ca^{2+} channels. Annu Rev Cell Dev Biol 16:521-555.

Chang YC, Gottlieb DI. 1988. Characterization of the proteins purified with monoclonal antibodies to glutamic acid decarboxylase. J Neurosci 8:2123–2130.

Chemin J, Monteil A, Perez-Reyes E, Bourinet E, Nargeot J, Lory P. 2002. Specific contribution of human T-type calcium channel isotypes (α1G, α1H and α1I) to neuronal excitability. J Physiol 540: 3-14.

Contreras D, Curro Dossi R, Steriade M. 1993. Electrophysiological properties of cat reticular thalamic neurones in vivo. J Physiol (Lond) 470:273-294.

Destexhe A, Neubig M, Ulrich D, Huguenard J. 1998. Dendritic low-threshold calcium currents in thalamic relay cells. J Neurosci 18:3574-3588.

Ernst WL, Zhang Y, Yoo JW, Ernst SJ, Noebels JL. 2009. Genetic enhancement of thalamocortical network activity by elevating α1G mediated low-voltage-activated calcium current induces pure absence epilepsy. J Neurosci 29:1615-1625.

Fiala JC. 2005. Reconstruct: a free editor for serial section microscopy. J Microscopy 218:52-61.

Gabbott PLA, Bacon SJ. 1994. Two type of interneurons in the dorsal lateral geniculate nucleus of the rat: a combined NADPH diaphorase histochemical and GABA-immunocytochemical study. J. Comp. Neurol. 350: 281-301.

Hanson JE, Smith Y. 2002. Subcellular distribution of high-voltage-activated calcium channel subtypes in rat globus pallidus neurons. J Comp Neurol 442:89-98.

Hildebrand ME, Isope P, Miyazaki T, Nakaya T, Garcia E, Feltz A, Schneider T, Hescheler J, Kano M, Sakimura K, Watanabe M, Dieudonne S, Snutch TP. 2009. Functional coupling between mGluR1 and Cav3.1 T-type calcium channels contributes to parallel fibre-induced fast calcium signaling within purkinje cell dendritic spines. J Neurosci 31:9668-9682.

Huguenard JR. 1996. Low-threshold calcium currents in central nervous system neurons. Annu Rev Physiol 58:329-348.

Jahnsen H, Llinás R. 1984. Electrophysiological properties of guinea-pig thalamic neurones: an in vitro study. J Physiol 349:205-226.

Jones SW. 1998. Overview of voltage dependent calcium channels. J Bioenerg Biomemb 30:299-312.

Jones EG. 2007. The Thalamus, 2nd Ed. Cambridge University Press, New York.

Kim D, Song I, Keum S, Lee T, Jeong MJ, Kim SS, McEnery MW, Shin HS. 2001. Lack of burst firing of thalamocortical relay neurons and resistance to absence seizures in mice lacking α1G T-type calcium channels. Neuron 31:35-45.

Kovács K, Sík A, Ricketts C, Timofeev I. 2009. Subcellular distribution of low-voltage activated T-type Ca^{2+} channel subunits (Cav3.1 and Cav3.3) in reticular thalamic neurons of the cat. J Neurosci Res 88:448-460.

Kulik A, Nakadate K, Hagiwara A, Fukazawa Y, Lujan R, Saito H, Suzuki N, Futatsugi A, Mikoshiba K, Frotscher M, Shigemoto R. 2004. Immunocytochemical localization of the α1A subunit of the P/Q- type calcium channel in the rat cerebellum. Eur J Neurosci 19:2169-2178.

Lee J, Kim D, Shin HS. 2004. Lack of delta waves and sleep disturbances during non-rapid eye movement sleep in mice lacking α1G-subunit of T-type calcium channels. Proc Natl Acad Sci USA 101:18195–18199.

Lein ES et al. 2007. Genome-wide atlas of gene expression in the adult mouse brain. Nature 445:168–176.

Leresche N, Hering J. Lambert RC. 2004. Paradoxical potentiation of neuronal T-type Ca^{2+} current by ATP at resting membrane potential. J Neurosci 24:5592–5602.

Lieberman AR, Webster KE. 1974. Aspects of the synaptic organization of intrinsic neurons in the dorsal lateral geniculate nucleus. An ultrastructural study of the normal and of the experimentally deafferented nucleus in the rat. J Neurocytol 3:677–710.

Liu XB, Honda CN, Jones EG. 1995. Distribution of four types of synapse on physiologically identified relay neurons in the ventral posterior thalamic nucleus of the cat. J Comp Neurol 352:69-91.

Masugi-Tokita M, Shigemoto R. 2007. High-resolution quantitative visualization of glutamate and GABA receptors at central synapses. Curr Opin Neurobiol 17:387–393.

McCormick DA, Pape HC. 1988. Acetylcholine inhibits identified interneurons in the cat lateral geniculate nucleus. Nature 334:246–248.

McKay BE, McRory JE, Molineux ML, Hamid J, Snutch TP, Zamponi GW, Turner RW. 2006. Ca(V)3 T-type calcium channel isoforms differentially distribute to somatic and dendritic compartments in rat central neurons. Eur J Neurosci. 24:2581–2594.

Munsch T, Budde T, Pape HC. 1997. Voltage activated intracellular calcium transients in thalamic relay cells and interneurons. Neuroreport 8:2411-2418.

Murphy PC, Sillito AM. 1987. Corticofugal feedback influences the generation of length turning in the visual pathway. Nature 329:727-729.

Ohara PT, Lieberman AR, Hunt SP, Wu JY. 1983. Neural elements containing glutamic acid decarboxylase in the dorsal lateral geniculate nucleus of the rat; immunohistochemical studies by light and electron microcopy. Neuroscience 8:189-211.

Ohara PT, Havton LA. 1994. Dendritic architecture of rat somatosensory thalamocortical projection neurons. J Comp Neurol 341:159-171.

Pape HC, Budde T, Mager R, Kisvarday ZF. 1994. Prevention of Ca^{2+}-mediated action potentials in GABAergic local circuit neurones of rat thalamus by a transient K^+ current. J Physiol (Lond) 478:403–422.

Pape HC, McCormick DA. 1995. Electrophysiological and pharmacological properties of interneurons in the cat dorsal lateral geniculate nucleus. Neuroscience 68:1105–1125.

Park JY, Kang HW, Moon HJ, Huh SU, Jeong SW, Soldatov NM, Lee JH. 2006. Activation of protein kinase C augments T-type Ca^{2+} channel activity without changing channel surface density. J Physiol (Lond) 577:513–523.

Paxinos G. 1995. The rat nervous system, 2nd Ed. Sydney: Academic press.

Perez-Reyes E, Cribbs LL, Daud A, Lacerda AE, Barclay J, Williamson MP, Fox M, Rees M, Lee J-H. 1998. Molecular characterization of a neuronal low-voltage-activated T-type calcium channel. Nature 391:896-900.

Perez-Reyes E. 2003. Molecular physiology of low-voltage-activated T-type calcium channels. Physiol Rev 83:117-161.

Pirchio M, Lightowler S, Crunelli V. 1990. Postnatal development of the T calcium current in cat thalamocortical cells. Neuroscience 38:39–45.

Rhodes PA, Llinas R. 2005. A model of thalamocortical relay cells. J Physiol (Lond) 565:765-781.

Richter TA, Kolaj M, Renaud LP. 2006. Heterogeneity in low voltage-activated Ca^{2+} channel-evoked Ca^{2+} responses within neurons of the thalamic paraventricular nucleus. Eur J Neurosci 24:1316-1324.

Robson JA. 1993. Qualitative and quantitative analysis of the patterns of retinal input to neurons in the dorsal lateral geniculate nucleus of the cat. J Comp Neurol 334:324-336.

Sherman SM, Guillery RW. 1998. On the actions that one nerve cell can have on another: distinguishing "drivers" from "modulators". Proc Natl Acad Sci USA 95:7121-7126.

Song I, Kim D, Choi S, Sun M, Kim Y, Shin HS. 2004. Role of the α1G T-type calcium channel in spontaneous absence seizures in mutant mice. J Neurosci 24:5249–5257.

Steriade M, Llinas RR. 1988. The functional state of the thalamus and the associated neuronal interplay. Physiol Rev 68:649-742.

Talley EM, Cribbs LL, Lee J, Daud A, Perez-Reyes E, Bayliss DA. 1999. Differential distribution of three members of a gene family encoding low voltage-activated (T-type) calcium channels. J Neurosci 19:1895-1911.

Williams SR, Stuart GJ. 2000. Action potential backpropagation and somato-dendritic distribution of ion channels in thalamocortical neurons. J Neurosci 20:1307-1317.

Yunker AMR, Sharp AH, Sundarrad S, Ranganathan V, Copeland TD, McEnery MW. 2003. Immunological characterization of T-type voltage dependent calcium channel Cav3.1 (alpha1G) and Cav3.3 (alpha1I) isoforms reveal differences in their localization, expression and neural development. Neuroscience 117:321-335.

Zhan XJ, Cox CL, Sherman SM. 2000. Dendritic depolarization efficiently attenuates Low-threshold calcium spikes in thalamic relay cells. J Neurosci 20:3909-3914.

Zhang Y, Mori M, Burgess DL, Noebels JL. 2002. Mutations in high-voltage-activated calcium channel genes stimulate low-voltage-activated currents in mouse thalamic relay neurons. J Neurosci 22:6362–6371.

Zhou Q, Godwin DW, O'Malley DM, Adams PR. 1997. Visualization of calcium influx through channels that shape the burst and tonic firing modes of thalamic relay cells. J Neurophysiol 77:2816-2825.

Zhu JJ, Lytton WW, Xue JT, Uhlrich DJ. 1999. An intrinsic oscillation in interneurons of the rat lateral geniculate nucleus. J Neurophysiol 81:702–711.

Zhuravleva SO, Kostyuk PG, Shuba YM. 2001. Subtypes of low voltage-activated Ca^{2+} channels in laterodorsal thalamic neurons: possible localization and physiological roles. Eur J Physiol 441:832-839.

Zomorrodi R, Kröger H, Timofeev I. 2008. Modeling thalamocortical cell: impact of Ca^{2+} channel distribution and cell geometry on firing pattern. Front Comput Neurosci 2:5. doi:10.3389/neuro.10.005.2008.

FIGURE LEGENDS

Figure 1. α1G immunoreactivity in the mouse thalamus

Light microscopic immunoperoxidase staining for α1G in the coronal brain slice showed intense immunoreactivity in several thalamic nuclei in the wild-type (WT) mouse but not in the α1G knock-out (KO) mouse. APT, anterior pretectal nucleus; dLGN, dorsal lateral geniculate nucleus; LP, lateral posterior thalamic nucleus; PF, parafascicular nucleus; VB, Ventrobasal nucleus; vLGN, ventral lateral geniculate nucleus. Scale bar, 250 μm.

Figure 2. Immunoreactivity for α1G was found exclusively in postsynaptic elements in the dLGN

Immunoperoxidase staining and immunogold labeling for α1G in the mouse dLGN were investigated by electron microscopy. The peroxidase reaction end product was observed exclusively in the dendrites but not in the presynaptic compartments (A). Electron micrographs showing the localization of the immunogold particles in the dendritic regions (B) and soma (C) demonstrate that the immunoparticles were found not only in close proximity to the plasma membrane (arrows) but also deep in the cytoplasm (arrowheads). Scale bars, 500 nm in A, 800 nm in B, 1.5 μm in C. a, presynaptic axons; c, cytoplasm; d, dendrite; n, nucleus.

Figure 3. Immunogold particles for α1G were associated with membrane structures

Location of immunoparticles for α1G was measured in relation to the nearest membrane structures. The values were allocated to 5-nm-wide bins and expressed as count. The frequency distribution of the particles (n = 179) plotted against their distance from the nearest membrane structure showed a single peak lying at 10-15 nm (mean = 16.6 nm and median = 14.6 nm). Approximately 95% of the immunoparticles were within 42 nm from the membranes, suggesting that the particles were bound to epitopes present in the cellular membranes.

Figure 4. Proportion of plasma membrane-bound immunoparticles for α1G

Bar graphs showing relative proportions of the plasma membrane-bound particles which were estimated in 28 reconstructed dendrites and analyzed in relation to the diameter of individual profiles. A total of 1284 immunoparticles were analyzed. Note that the large-caliber dendrites showed higher proportion of internal labeling (see text). In total, 46.1% of the particles were plasma membrane-bound whereas the rest of the particles (53.9%) were located intracellularly.

Figure 5. Three-dimensional reconstruction of labeled dendrites

Consecutive serial pictures show α1G immunogold labeling in the small-caliber dendrite (A-D) and in the large-caliber dendrite (E-H). Four dendrites with membrane-bound particles reconstructed from 28 serial electron micrographs are shown (I-L). Asymmetrical synapses (excitatory) are represented by red and symmetrical synapses (inhibitory) are represented by green. Particles in black represent particles facing towards the observer and particles in pink represent those on the opposite face of the dendritic arbor. The faint green synapse in K is located on the opposite face of the arbor. Note that the immunoparticles (total 132 particles) were distributed randomly over the dendritic plasma membrane without any noticeable preference to the synaptic sites. d, dendritic diameter; D, labeling density (particle/μm^2). Scale bars = 200 nm in A-D, 500 nm in E-H, 500 nm in I-L.

Figure 6. α1G immunoparticles were observed uniformly over the somatodendritic domains of the plasma membrane

(A) Density of immunogold particles for α1G associated with the plasma membrane was measured in serial section electron micrographs (n = 28 for dendrites; n = 3 for somata) and plotted against the diameter of individual profiles. The diamond tiles represent the labeling densities of individual relay cell dendrites, and the rectangle represents the average labeling density in the relay cell soma. No correlation was observed between the dendritic diameter and the immunogold density (r = -0.209, *P* = 0.286). Note that there

was a large variability in the immunogold density even among the dendrites with similar dendritic diameters, and the variability was more pronounced in the small-caliber dendrites compared to the larger-caliber proximal dendrites. (B) Number of internal membrane-bound immunogold particles for α1G was divided by the cross-sectional area of individual profiles and plotted against the diameter of the profile. The intracellular labeling density for α1G was highest at the proximal dendrites and decreased gradually towards the small-caliber dendrites. A positive correlation was found between the density of the α1G particles and the dendritic diameter ($r = 0.559$, $P = 0.002$, n = 28 for dendrites; n = 3 for somata).

Figure 7. GABAergic interneurons showed weaker immunoreactivity for α1G than putative relay cells in the dLGN

The expression of α1G in GABAergic interneurons was investigated by double immunoelectron microscopy for α1G and GAD. GAD immunoreactivity was visualized by a peroxidase reaction and that for α1G was visualized by immunogold particles. Consecutive images show a relay cell dendrite (r) and an interneuron dendrite (i) located adjacent to each other. Scale bar = 500 nm.

Figure 8. α1G expression level in interneurons was lower than that in relay cells in the dLGN

Bar graphs showing the average densities of the plasma membrane-bound immunogold particles for α1G in the dendrites, classified into three groups according to their diameter (< 0.5 μm, 0.5-1 μm, > 1 μm), and somata of the relay cells (open bar; n = 22 and 3 for dendrite and soma, respectively) and GABAergic interneurons (closed bar; n = 19 and 3 for dendrite and soma, respectively). The labeling densities in the interneurons were similar over different dendritic compartments (ANOVA, $P = 0.775$) and significantly lower than those in the relay cell ($P < 0.001$, Mann-Whitney U-test). In corroboration with the observation made from the single labeling experiment, no somatodendritic gradient of α1G immunogold particle was observed in the plasma

membrane of the relay cells. Note that the relatively large magnitude of error bars (SEM) associated with each of the compartments suggests a considerable variability of the immunogold labeling density among the profiles with similar dendritic diameters.

Supporting figure 1. A light micrograph showing α1G immunoreactivity in various thalamic nuclei. Note that the α1G immunoreactivity is observed in various thalamic relay nuclei but not in the reticular thalamic nucleus (TRN). In contrast to the intense immunoreactivity observed in the thalamic relay nuclei of the wild-type (WT) mouse, no immunoreactivity is detected in the brain sections obtained from the knock-out (KO) mouse. LD, laterodorsal thalamic nucleus; LHb, lateral habenular nucleus; MD, mediodorsal thalamic nucleus; MHb, medial habenular nucleus; TRN, reticular thalamic nucleus; Po, posterior thalamic nucleus; VL, ventrolateral thalamic nucleus; VM, ventromedial thalamic nucleus; VPL, ventral posterolateral thalamic nucleus; VPM, ventral posteromedial thalamic nucleus; ZI, zona incerta. Scale bar = 0.5 mm.

Supporting figure 2. The immunolabeling is specific to α1G molecules.
At the light microscopic level, the intense immunolabeling observed in the dLGN from the WT animal (A) disappeared in the corresponding section obtained from KO animal (B). Electron micrograph in C shows selective immunogold labeling to the postsynaptic profiles in WT tissue. Consistent with the lack of labeling in the KO animal at the light microscopic level (B), the LGN of α1G KO animal showed no α1G immunoreactivity at the electron microscopic level (D). Scale bars = 250 μm in A, 500 nm in B and C. a, presynaptic axons; d, dendrite.
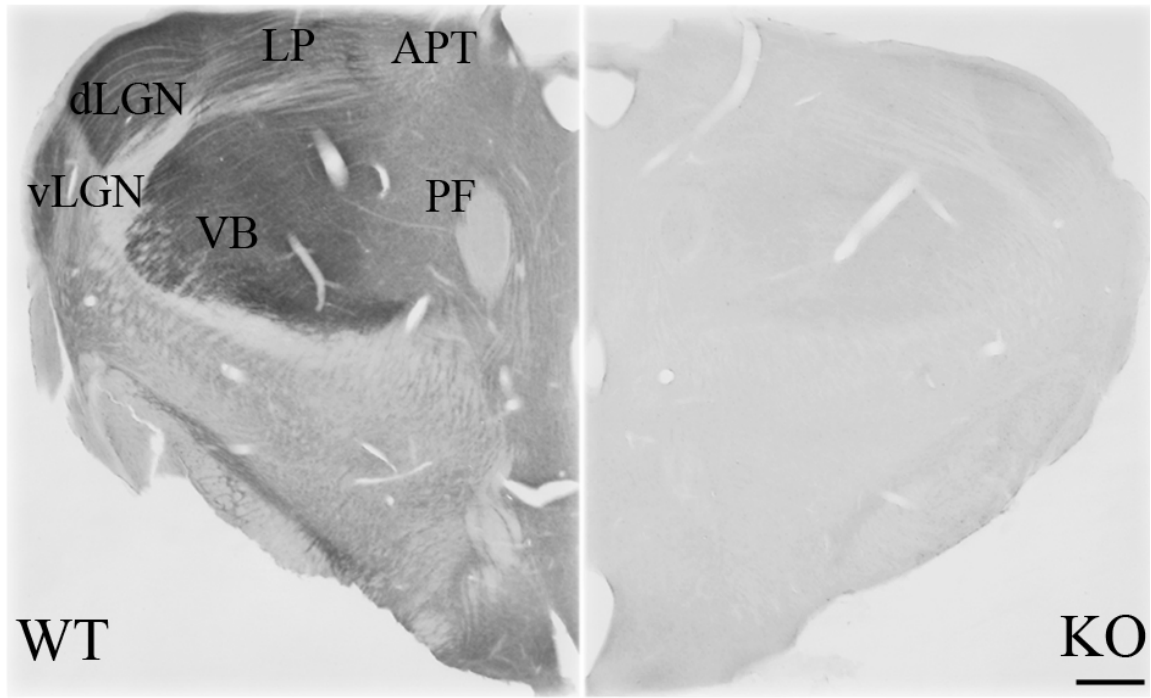
Table 1

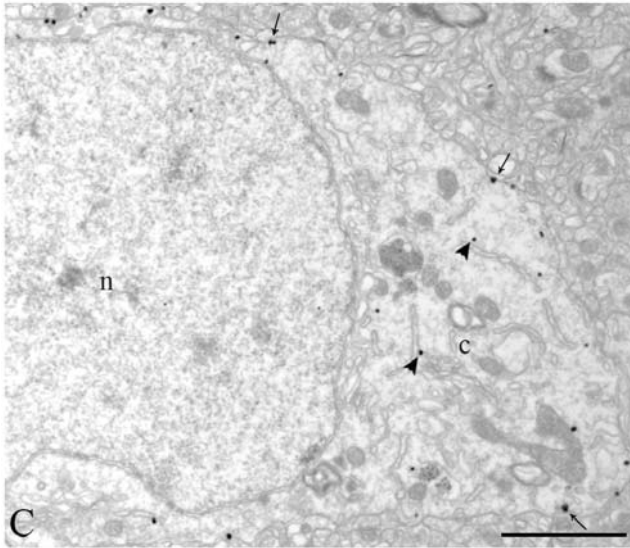| Target molecule	Code# in original lab or supplier	Host animal and clonality	Developer or supplier	Epitope amino acid residues	Optimal dilution
α1G subunit of T-type Ca^{2+} channel	N/A	Guinea pig Polyclonal Affinity purified	Dr. Masahiko Watanabe	Amino acid residues 2269-2283 of the mouse Cav3.1 gene (CAI25956)	1 μg / ml
Glutamic acid decarboxylase (GAD)	MAB351	Mouse Monoclonal (Affinity purified IgG)	Chemicon	Purified rat brain GAD (Chang and Gottlieb,1988)	1 μg / ml

N/A, Not applicable

Figures

Figure 1

Figure 2

Figure 3

Figure 4

d = 0.39
D = 2.99

d = 0.43
D = 3.47

d = 1.57
D = 3.56

d = 1.58
D = 4.34

Figure 5

A — Plasma membrane
r = - 0.209
Linear density (particle/µm)

B — Internal membrane
Density (particle/µm²)
r = 0.559
Dendritic diameter (µm)
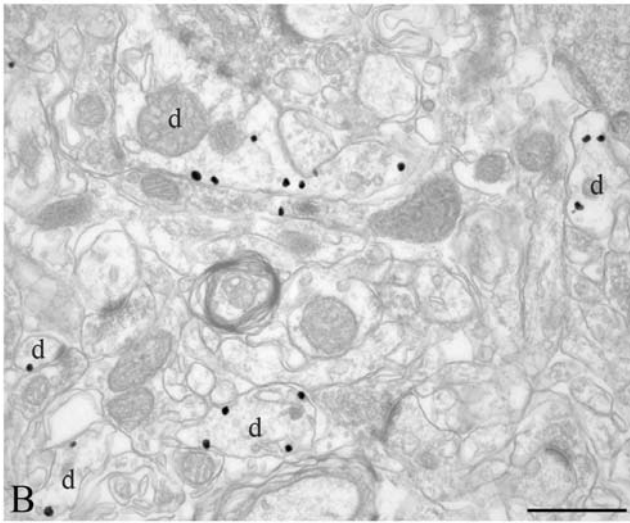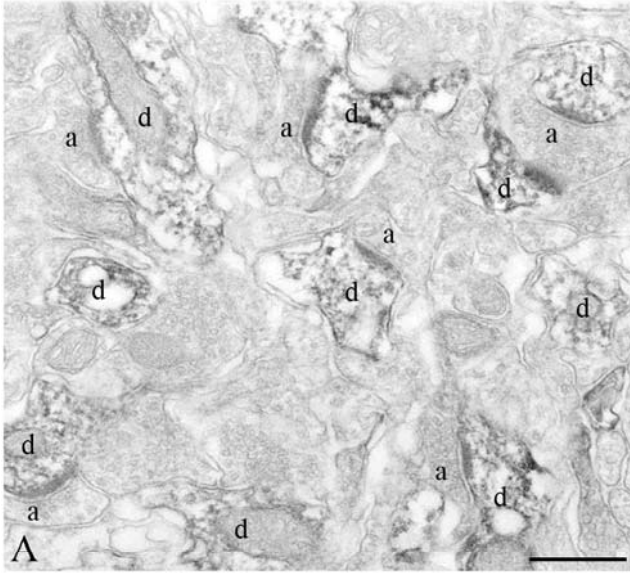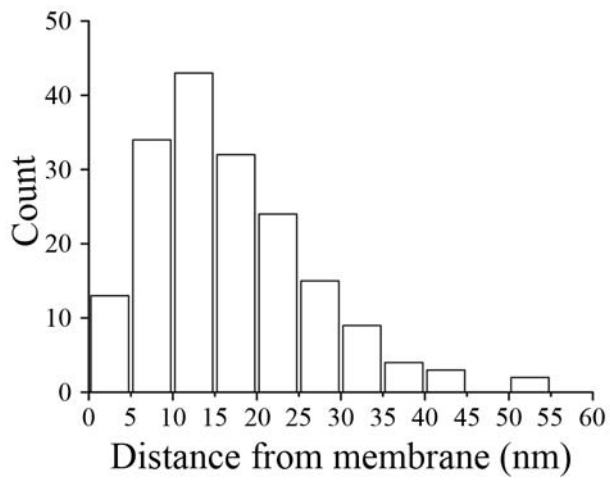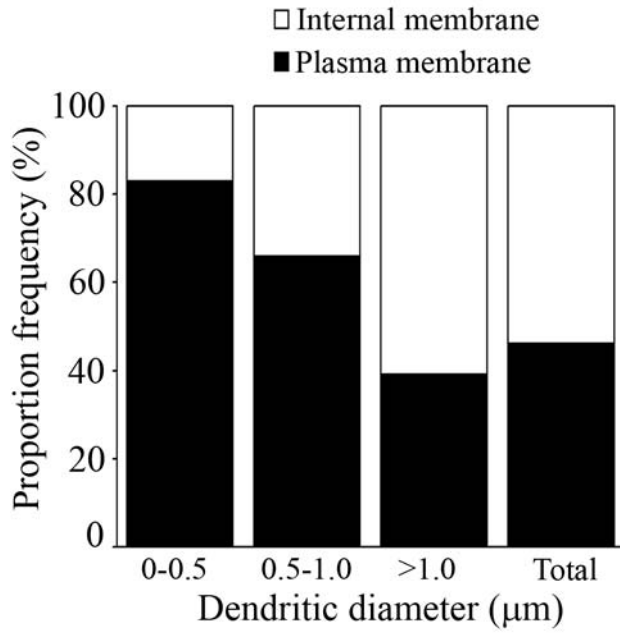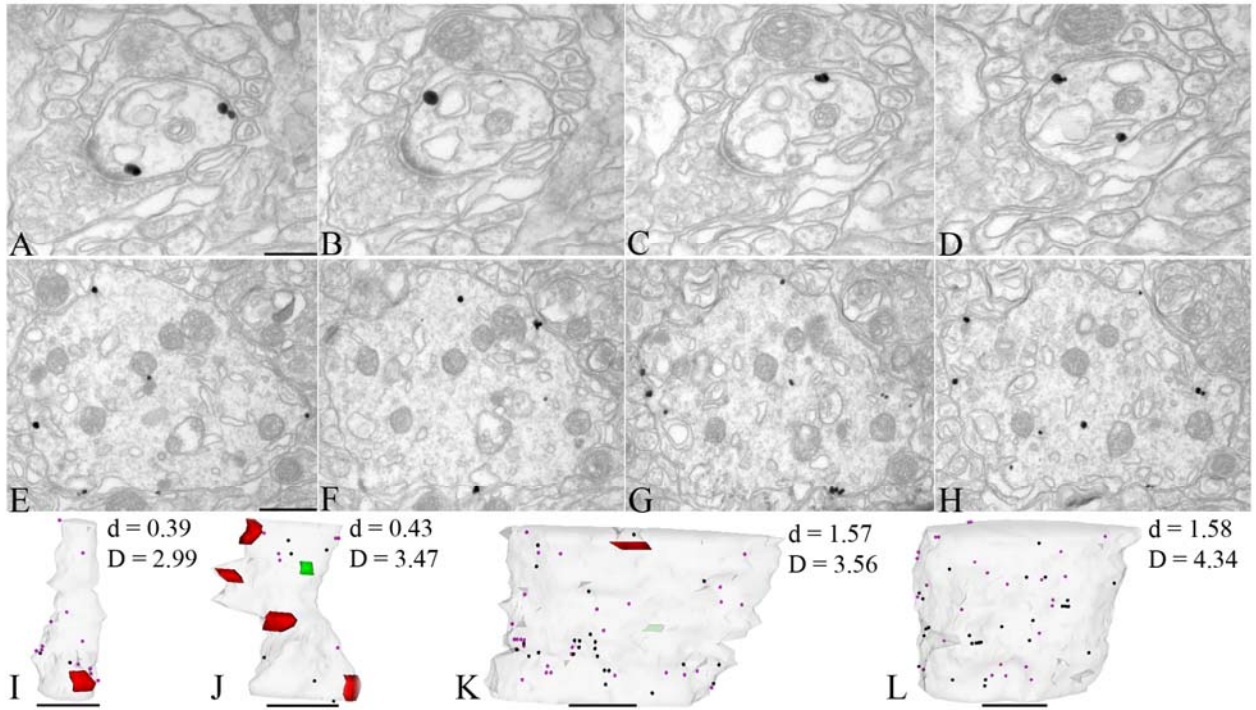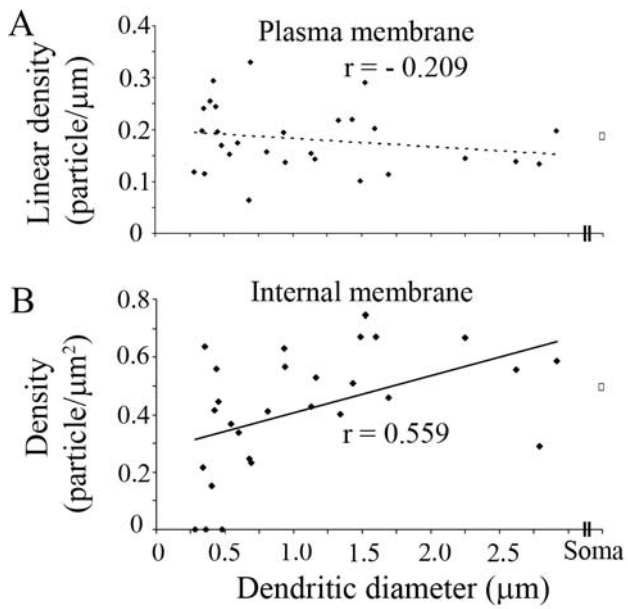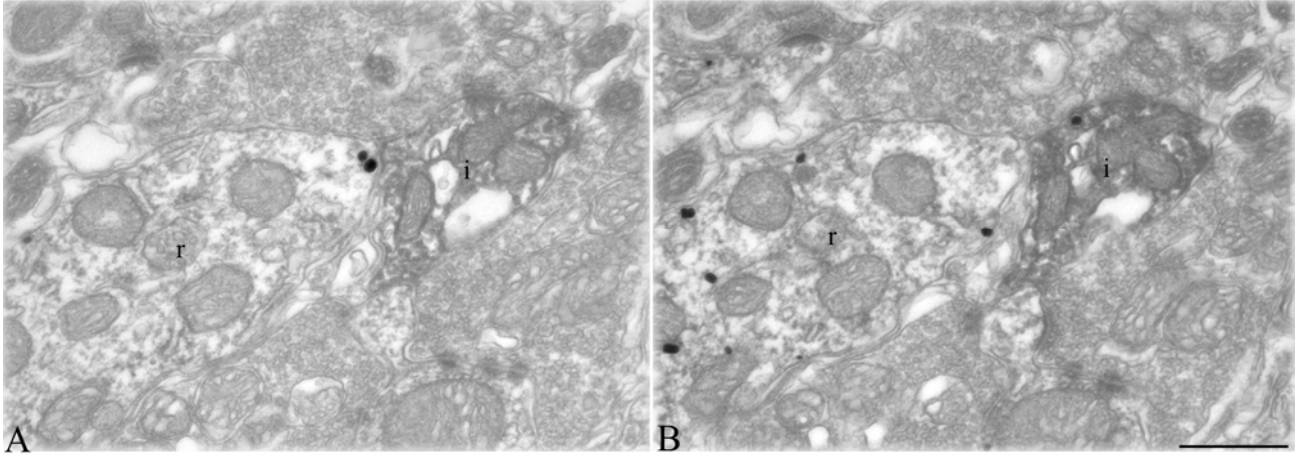
Figure 6
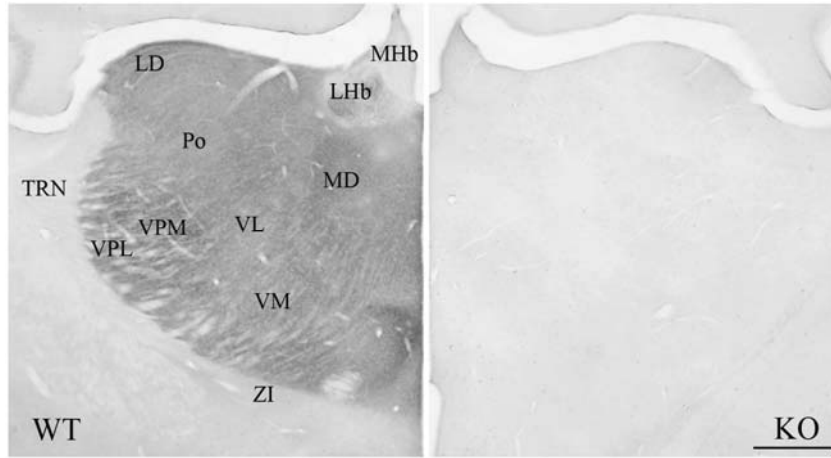
Figure 7

Figure 8

Supporting figure 1
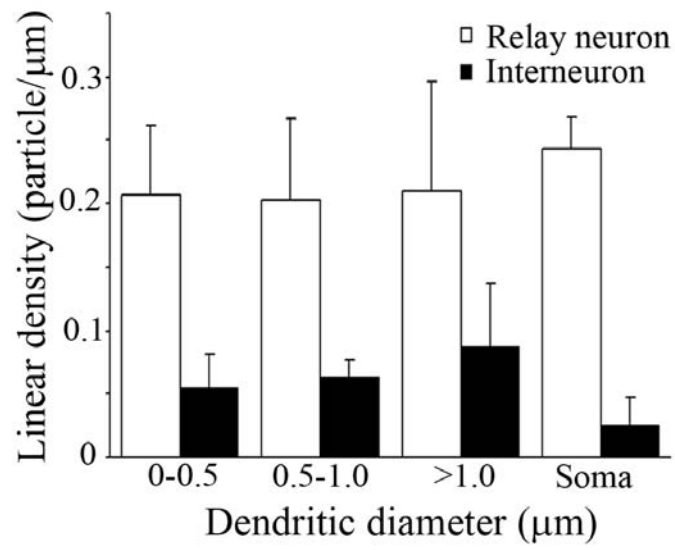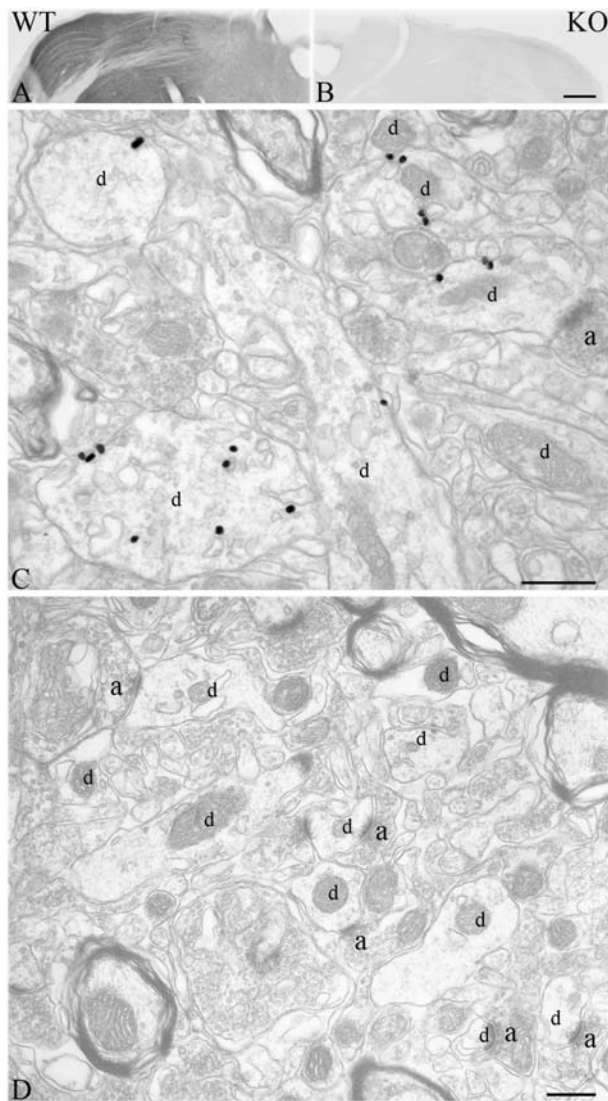

Supporting figure 2

Chapter 2: Quantitative regional and ultrastructural localization of the Ca$_v$2.3 subunit of R-type calcium channels in the mouse brain

Abstract

R-type calcium channels (RTCC) are well known for their role in synaptic plasticity, but little is known about their subcellular distribution across various neuronal compartments. Using subtype-specific antibodies, I characterized the regional and subcellular localization of Ca$_v$2.3 at both light and electron microscopic levels. Ca$_v$2.3 immunogold particles were found to be predominantly presynaptic in the interpeduncular nucleus, but postsynaptic in other brain regions. Serial section analysis of electron microscopic images from the hippocampal CA1 revealed a higher density of immunogold particles in the dendritic shaft plasma membrane compared with the pyramidal cell somata. However, the labeling densities were not significantly different among the apical, oblique or basal dendrites. Immunogold particles were also observed over the plasma membrane of dendritic spines, including both synaptic and extrasynaptic sites. Individual spine heads contained < 20 immunogold particles, with an average density of ~ 260 immunoparticles per μm^3 spine head volume, in accordance with the density of RTCCs estimated using calcium imaging (Sabatini and Svoboda, 2000). The Ca$_v$2.3 density was variable among similar-sized spine heads and did not correlate with the density in the parent dendrite, implying that spines are individual calcium compartments operating autonomously from their parent dendrites.

Introduction

The R-type calcium channel (RTCC) is a unique member of voltage-gated calcium channel (VGCC) subtypes, as its biophysical properties, such as the membrane voltage and the kinetics for channel activation and inactivation, are distinct from those of typical high-voltage- activated (P/Q-, N-, and L-type) or low-voltage-activated classes of VGCCs (T-type) (Soong et al., 1993; Williams et al., 1994). Although in some brain regions the molecular identity of RTCC remains somewhat controversial (Tottene et al., 2000; Wilson et al., 2000), the $Ca_v2.3$ subunit has been shown to mediate the RTCC (Sochivko et al., 2002; Giessel and Sabatini, 2011) current in the hippocampus. Among the ten VGCC subtypes, the RTCC has attracted a special attention in recent years because of its role in neurotransmitter release (Wu et al., 1999; Gasparini et al., 2001), hippocampal synaptic plasticity (Yasuda et al., 2003; Takahashi and Magee, 2009), and functional specificity over other VGCC subunits to dampen synaptic potentials by activating SK channels (Bloodgood and Sabatini, 2007). However, the subcellular locus of $Ca_v2.3$ mediated calcium signaling has not yet been identified.

In situ hybridization studies show a robust expression of $Ca_v2.3$ messenger RNA in the hippocampus (Soong et al., 1993; Williams et al., 1994), but the identity of the labeled cells and the protein localization cannot be fully characterized by this technique. Similarly, the subcellular localization of the $Ca_v2.3$ protein in hippocampal neurons remains inconsistent with reports of prominent somatic expression (Yokoyama et al., 1995), dendritic localization (Day et al., 1996) and even selective localization to dendritic spines of CA1 pyramidal cells (Bloodgood and Sabatini, 2007). To resolve inconsistencies in $Ca_v2.3$ localization, a quantitative immunolabeling study with highly specific antibodies to $Ca_v2.3$ is indispensible.

Previous calcium imaging studies (Svoboda et al., 1996, Sabatini et al., 2002) have shown that dendritic shafts and spines operate in a functionally independent manner. It is reported that synaptic plasticity is variable among the spines (Matsuzaki et al., 2004) and calcium ions often exert their influence locally in neurons (for review, see Augustine et al., 2003). The existence of calcium microdomains suggests that calcium channels may not be distributed randomly and are more likely localized into defined membrane

compartments. Hence, it is important to localize VGCC at a high spatial resolution by means of immunogold electron microscopy studies.

In this study, I used a specific antibody against the RTCC $Ca_v2.3$ subunit to study the regional distribution in the mouse brain and to perform quantitative ultrastructural localization in the hippocampus. Apart from the predominant presynaptic expression in the interpeduncular nucleus, $Ca_v2.3$ immunogold particles were mostly distributed postsynaptically in other regions. In dendritic spines of hippocampal pyramidal cells, $Ca_v2.3$ immunogold particles were mainly observed in extrasynaptic plasma membrane, suggesting a preferential role of $Ca_v2.3$ Ca^{2+} signals in the activation of downstream signaling molecules located in extrasynaptic sites. Furthermore, I demonstrate that the $Ca_v2.3$ density in the spines does not correlate with that in the parent dendrites, supporting the view that spines are biochemical compartments that operate independently from their parent dendrites.

Materials and methods
Animals

In this study, 2-month-old female guinea pigs (n = 10), 2- to 3-month-old adult male C57BL/6 mice (n = 10), and age-matched, sex-matched $Ca_v2.3$ knockout (KO) mice (n = 7) and postnatal day 20 rats (n = 2) were used. Methodological details on the generation of $Ca_v2.3$ KO mouse have been reported previously (Saegusa et al., 2000; Pereverzev et al., 2002). Animals were raised in a normal light/dark cycle in the authors' institutional animal facilities and were fed with food and water *ad libitum*. All the experiments were performed according to the institutional guidelines for animal welfare and the experimental protocol was approved by the animal care and use committees of the authors' institutions.

Antibody production and Western blotting

Guinea pig polyclonal $Ca_v2.3$ antibodies against C-terminal sequence of mouse $Ca_v2.3$ were generated using immunizing peptides directed against four different epitopes corresponding to the amino acid residues 2001 - 2017 (epitope 1), 2069 - 2087 (epitope 2), 2108 - 2127 (epitope 3) and 2231 - 2248 (epitope 4) of the mouse $Ca_v2.3$ protein

(Q61290, Fig. 1F). Each antigen (0.5 mg) or a mixture of four peptides (0.5 mg, referred to hereafter as pan-epitope antibody) was conjugated to 2 mg of keyhole limpet haemocyanin (KLH) for immunization. Affinity purification of the sera was performed by using a mixed antigen peptide column (Aldevron). The pan-epitope and the epitope 2 antibodies were found to be suitable for immunohistochemistry.

Lysates from hippocampus and cortex of wild type (WT) and age-matched $Ca_v2.3$ KO mice were prepared by homogenization with a glass-Teflon homogenizer in RIPA buffer [50 mM Tris-HCl (pH 8.0), 150 mM NaCl, 1 mM EDTA, 1 % (v / v) NP-40, 0.5 % (w / v) sodium deoxycholate, 0.1% (w / v) SDS], including protease inhibitor mixture (Sigma Aldrich) and 1 mM phenylmethylsulfonyl fluoride. Homogenates were centrifuged (14000 relative centrifugal force, 15 min at 4°C) and the resulting supernatant was heated with loading buffer, including 20 mM DTT, at 37°C for 30 min. Fifty micrograms of each sample were subjected to SDS-PAGE and Western blotting according to standard procedures. Affinity purified guinea-pig polyclonal antibodies against the pan-epitope (1 µg / ml) or the $Ca_v2.3$ epitope 2 (1 µg / ml) were used. After primary antibody incubation, sequential incubation with goat anti-guinea pig IgG-HRP (1:5000 dilution, Santa Cruz, Germany) was performed. Immunoblots were visualized by enhanced chemiluminescence reagent captured on x-ray film.

Tissue processing for light and electron microscopy

Animal anesthetization, fixation, and tissue processing for light microscopy (LM) and pre-embedding immunoelectron microscopy (EM) were performed as described previously (Kulik et al., 2004; Parajuli et al., 2010). Deeply anaesthetized animals were transcardially perfused through the ascending aorta with 25 mM phosphate-buffered saline (PBS, pH 7.4) for 1 minute. This was followed by a fixative containing 4 % paraformaldehyde and 15 % saturated picric acid made up in 0.1 M phosphate buffer (PB; pH 7.4) for 12 minutes at a flow rate of 5 ml / min. For electron microscopy, 0.05 % glutaraldehyde was freshly added to the fixative solution. After perfusion, brains were quickly removed from the skull, washed briefly with PB, embedded in 1 % agarose, and coronally sectioned at 50 µm with a microslicer (VT-1000, Leica).

Sections for LM analysis were rinsed several times in PBS, and then incubated in a blocking solution containing 10 % normal goat serum (NGS; Vector Laboratories, Burlingame, CA) and 0.1 % Triton X-100 in PBS for 45 minutes. Sections were incubated overnight at 4^oC with an affinity-purified polyclonal antibody against $Ca_v2.3$ (1 - 2 µg / ml), made up in PBS containing 2 % NGS and 0.1 % Triton X-100, and were then washed in PBS and incubated with biotinylated goat anti-guinea pig IgG antibody (1 : 200; Vector Laboratories) at room temperature for 1 hour. The sections were washed in PBS, and reacted with an avidin-biotinylated horseradish peroxidase complex (1:100 ABC-Elite; Vector Laboratories) made up in PBS containing 0.1 % Triton X-100. After three washes in PBS and one in 50 mM Tris-HCl buffer (TB; pH 7.4), the peroxidase activity was visualized by incubating sections in TB containing 0.025 % 3, 3'-diaminobenzidine tetrahydrochloride (Dojindo Molecular technologies) and 0.003 % hydrogen peroxide. Sections were then transferred onto gelatin-coated glass slides and dehydrated through a graded series of ethanol, followed by xylene and finally mounted under glass coverslips. Photomicrographs of the coronal sections were captured using a BX50 microscope equipped with a DP70 digital camera (Olympus, Tokyo, Japan).

For immunogold EM labeling, 50-µm-thick cyroprotected sections were freeze-thawed. Subsequently, sections were blocked for 45 minutes in 20 % NGS in Tris-buffered saline (TBS) and incubated overnight at 4^oC in primary antibody (1 - 2 µg / ml) made up in TBS, pH 7.4, containing 1 % NGS. After washing, the sections were incubated with 0.8 nm gold-coupled (Aurion) or 1.4 nm gold-coupled (Nanoprobes) anti-guinea pig secondary antibodies diluted in TBS at a ratio of 1:100. After washing, the sections were postfixed in 1 % glutaraldehyde for 10 minutes, followed by silver enhancement of the immunogold particles using either an Aurion R-gent SE (Aurion) or a HQ silver (Nanoprobes) EM intensification kit. Sections were then postfixed with 1 % osmium tetroxide for 30 - 40 minutes, *en bloc* counterstained with 1 % uranyl acetate for 30 minutes, and dehydrated in graded ethanol series followed by propylene oxide. Sections were infiltrated overnight at room temperature in Durcapan resin (Sigma-Aldrich) and transferred to glass slides for flat embedding. After resin curing at 60^oC, the trimmed tissues from the region of interest were re-embedded in Durcapan resin blocks for ultrathin sectioning. Serial 70- nm-thick sections were cut from the surface (within 3

μm depth) of the samples and were collected in pioloform-coated single slot copper grids. Images were captured with a CCD camera connected to a Philips EM208S transmission electron microscope.

Identification of profiles

The neuronal elements in the CA1 area can be differentiated from glial cells based on morphological criteria. Glial processes often have a highly irregular shape, and possess a pale cytoplasmic mass that contains many prominent dark glycogen granules and parallel bundles of intermediate filaments (Peters et al., 1991). A profile was judged as being a presynaptic terminal if its characteristics included synaptic vesicle accumulation, presence of presynaptic specializations, and rigid alignment of presynaptic membrane to its postsynaptic partner. Synapses were identified based on postsynaptic thickening and electron dense materials in the synaptic cleft (Peters et al., 1991). Pyramidal cell dendrites had symmetrical shaft synapses and asymmetrical synapses on spine heads with narrow, cylindrical neck like structures (for review, see Bourne and Harris, 2008). These spiny protrusions did not contain any mitochondria. Dendritic profiles lacking spiny protrusions and possessing numerous asymmetrical synapses on their shafts were identified as interneurons (Megias et al., 2001) and were omitted from the analysis.

Quantification of LM immunoreactivity

In order to obtain quantitative measure of LM immunoreactivity for $Ca_v2.3$, all images of WT and $Ca_v2.3$ KO brain sections were acquired under the same microscopic settings. Images were then uploaded to NIH ImageJ software, converted to 8-bit grayscale and inverted. Densitometric measurements were carried out at three different areas within individual regions of interest using the mean intensity measurement function of the software. Average background levels were determined by quantification from many areas in the KO mice. All WT measurements were corrected using the established KO baseline. These values were used to group nuclei into 5 expression categories as listed in Table 1.

The epitope 2 antibody was chosen for LM mapping because the pan antibody showed some non-specific staining in the stratum lucidum of the hippocampal CA3 area, cerebellum and inferior olive in the $Ca_v2.3$ KO tissues.

Immunogold quantification

Serially sectioned images were imported into the Reconstruct software (Fiala, 2005) and the image stacks were aligned. Plasma membranes of individual dendrites and spine heads were manually traced. To obtain a spine head volume, the total cross-sectional area of the closed contours, formed by manually delineating the head of a given complete spine, was multiplied by the section thickness (70 nm). The surface area was estimated as a product of the section thickness and effective plasma membrane length. The length of the imaginary line introduced at the plasma membrane discontinuity portion in the head-neck junction, while drawing the closed contours, was measured by using the trace tool function. This length was subtracted from the length of the closed contours to obtain an effective plasma membrane length. Dendritic diameter was obtained as an average of distance connecting the shortest elliptical axis of a given dendrite in each of the serial images. The calculated volume and the surface area of neuronal profiles were not corrected for tissue shrinkage that may occur during dehydration steps (Trommald et al., 1995).

In order to introduce uniformity for counting silver intensified immunogold particles, I applied stringent and constant measures. The average diameter of immunogold particles was roughly 20 - 25 nm. If a single immunogold particle was cut into two during ultrathin sectioning, this could lead to the visualization of two immunogold particles appearing in two consecutive sections. To avoid the possibility of overestimating, immunogold particles were counted as one if two immunogold particles appeared exactly at the same location in two consecutive sections. However, in such a case, I introduced a criterion that the diameter of one of the immunogold particles should be half or less than the average diameter of the silver intensified immunogold particles in the surrounding profiles.

Extensive approach of immunogold quantification on serial electron microscopic images was made using two adult WT mice, one P20 rat and one adult $Ca_v2.3$ KO mouse.

Conclusions drawn from the quantification were then confirmed in 5 more WT mice at the qualitative level. The electron micrographs from the strongly labeled specimens were used for quantitative analysis. In order to establish a baseline for background labeling, multiple serial sections were reconstructed from hippocampal CA1 and immunogold particles were counted in both WT and $Ca_v2.3$ KO brains from 334 μm^2 area of each. Quantification of immunogold particles in the hippocampus was performed using the pan antibody, rather than epitope 2, as the former gave stronger labeling in my experimental condition.

The chain lengths of the primary and secondary antibodies inherently constrain the spatial resolution of the pre-embedding immunogold labeling method. Thus, it is inevitable to see individual immunogold particles located at a slight distance away from the exact site of the antigen (Matsubara et al., 1996). In order to confirm the membrane origin of $Ca_v2.3$ labeling, I measured the perpendicular distances between the center of the individual gold particles (n = 238) and the center of nearest membranous structure. The measured distances were allocated to a bin width of 5 nm and the frequency of immunogold particles in each bin was counted. The histogram distribution gave a single peak between 15 - 20 nm (median = 16.24 nm, mean = 17.70 nm, and SD = 12.26 nm) and a long tail towards higher values. Approximately 95% of the immunogold particles were found to be located within 42 nm (mean + 2 × SD) of the cytoplasmic face of the membrane, and this distance was taken as a threshold for considering immunogold particles as being attached to the plasma membrane. This threshold distance is consistent with reports from earlier studies (Lorincz et al., 2002; Baldi et al., 2010; Parajuli et al., 2010).

The distance of immunogolds measured from the nearest edge of the PSD was expressed as negative value if particles were located along the plasma membrane within the main body of the PSD and as a positive value if immunogold particles were seen on the extrasynaptic plasma membrane. Higher positive values represent immunoparticles further away from the edge of the PSD.

Statistical analysis was conducted using SPSS (Chicago, IL) and the level for statistical significance was set at 0.05. Normality of the data was assessed by applying Shapiro-Wilk's W-test. Statistical evaluation of immunogold densities was performed

using the student's t-test, Mann-Whitney U-test or one-way ANOVA where appropriate. Correlation was examined by using Spearman's rank order test. All results are reported as mean ± SEM.

Results

Epitopes recognized by Ca$_v$2.3 antibodies

In order to identify the epitope(s) recognized by the pan-epitope antibody, each of the four antigenic peptides against Ca$_v$2.3 were separately incubated at a tenfold molar excess with the antibody for 30 minutes. The resulting adsorbed antibody was applied to the sections for LM immunohistochemistry. While sections immunostained by the pan-epitope antibody preadsorbed with antigenic peptides against epitope 1, 2 or 4 resulted in signal that was indistinguishable from control sections (sections stained by pan-epitope antibody alone), peptide 3 adsorbed pan-epitope antibody showed no clear immunostaining (Fig. 1A). Thus, these results clearly demonstrate that specific signal generated by the pan-epitope antibody is attributable to the recognition of epitope 3 region (amino acid residues: 2108-2127) of Ca$_v$2.3 (Fig. 1F).

Antibodies against each of the four epitopes were generated and their suitability for immunohistochemistry was determined. Antibodies against epitopes 1, 3 or 4 did not produce any specific staining for Ca$_v$2.3 (data not shown). However, the antibody against epitope 2 (amino acid residues: 2069-2087) gave a staining pattern (Figs. 1B, C) similar to that obtained by the pan-epitope antibody (Figs. 1Ea-d), which provides an additional evidence for the specificity the antibodies to Ca$_v$2.3.

Light microscopic immunohistochemistry and Western blotting for Ca$_v$2.3

Immunohistochemistry revealed that Ca$_v$2.3 was distributed ubiquitously throughout the brain at varying intensities among different regions as summarized in Table 1. The staining was more prominent in the forebrain compared to the midbrain and hindbrain. Neuropils of the olfactory tubercule, superficial layers of the cortex, hippocampus, lateral septum, striatum, nucleus accumbens, interpeduncular nucleus (IPN), and the central and basolateral amygdala showed more intense staining (Figs. 1B, Ea-d), whereas the staining intensity was moderate in areas such as the hypothalamus and

substantia nigra. The immunoreactivity in the thalamus, ventral tegmental area, raphe nucleus was low or close to background levels. The immunohistochemical distribution of $Ca_v2.3$ correlates very well with the previously published *in situ* hybridization results (Soong et al., 1993; Williams et al., 1994; Allen brain atlas, Lein et al., 2007) except for some regions such as the medial habenula, IPN and the dorsal raphe nucleus. The *in situ* data show $Ca_v2.3$ mRNA in the medial habenula with no transcript in the IPN, which was completely opposite of immunoreactivity. It is interesting to note that neurons in the medial habenula primarily project to the IPN and thus presynaptic targeting of $Ca_v2.3$ in this locus can be inferred.

A remarkable difference in the intensity of immunoreactivity was seen between the CA1 and CA3 areas (Fig. 1C) of the hippocampus. In sharp contrast to the strong $Ca_v2.3$ immunoreactivity in the CA1 area, only a faint immunostaining could be observed in dendritic layers of the CA3 area. The distribution of immunoreactivity for $Ca_v2.3$ subunit in the CA3 field was not homogenous throughout the dendritic extent but rather enriched in the stratum oriens (SO) and stratum lucidum. In the CA1 area, the neuropil in the SO displayed stronger immunoreactivity than the neuropil in the proximal part of the stratum radiatum (PSR) and stratum lacunosum moleculare (slm). In the dentate gyrus, the staining intensity was similar throughout the molecular layer. The immunoreactivity in somata of granule cells was barely detected. The pattern and intensity of immunoreactivity detected in the hippocampus and other brain regions in WT sections (Figs. 1A-C, Ea-d) disappeared in tissues obtained from $Ca_v2.3$ KO animals (Figs. 1Ee and f). However, in the stratum lucidum, a faint immunoreactivity was still evident in $Ca_v2.3$ KO sections using the pan, but not epitope 2, antibody. This was likely due to the cross reactivity of the pan antibody with other protein(s) in this region.

The specificity of the pan and epitope 2 antibodies was further confirmed by Western blot analysis of hippocampal and cortical lysates made from both WT and $Ca_v2.3$ KO mice. A 250 kDa band, corresponding to the predicted molecular weight (Soong et al., 1993), disappeared in the KO lysate (Fig. 1D).

General description of the electron microscopic localization of immunogold particles

The ultrastructural localization of $Ca_v2.3$ was performed using the pre-embedding immunogold labeling methods. Both pan-epitope and epitope 2 antibodies produced identical patterns of immunostaining in the brain regions examined. Images were taken from the CA1, cortex and amygdala using the pan antibody, and the striatum, CA3 stratum lucidium and the interpeduncular nucleus using the epitope 2 antibody.

As expected from the intracellular location of the epitopes recognized by the $Ca_v2.3$ antibodies, immunoparticles were localized intracellularly along the plasma membranes of both post- and presynaptic elements (Figs. 2-4, 7). Cytosolic labeling was sparse, but if present the immunogold particles were often observed in the vicinity of some intracellular membranous structures (data not shown). Immunogold particles along the plasma membrane were either observed as a discrete individual particle (Figs. 2-4, 7) or as clusters of two (for instance, Fig. 2C with epitope 2 antibody or Fig. 4D with pan-antibody).

The EM immunogold analysis in the hippocampus, neocortex, striatum, and amygdala revealed that the channel subunit is preferentially localized postsynaptically in dendritic shafts and spines and to a lesser extent in presynaptic compartments. Particles were diffusely distributed along the plasma membrane of dendrites and the spines without any preference to specialized membrane compartments (e.g. postsynaptic density, apposition to glial contact etc.). In the CA3 stratum lucidum, the immunogold particles were seen in the CA3 pyramidal cell dendrites, thorny excrescence spines and the mossy fiber terminals (Figs. 2D-F). In the mossy fibre terminals, particles could be seen both in the active zone (AZ) of the terminals (Fig. 2E) or remote from the presynaptic membrane specialization (Fig. 2F).

In contrast to the strong postsynaptic labeling in the other brain areas, immunogold particles were densely localized in the presynaptic boutons of the medial habenula (MHb) terminals in the interpeduncular nucleus (IPN, Figs. 2G-K). Labeling was observed both in the crest (arrows in Fig. 2G) and en passant S synapses (Figs. 2J, K), both of which in the IPN are shown to be derived from MHb fibres (Lenn et al., 1976). $Ca_v2.3$ immunogold particles were observed primarily in the extrasynaptic plasma

membrane and occasionally over the presynaptic AZ, indicating a distinct distribution pattern in comparison to Ca$_v$2.1 channels (Kulik et al., 2004; Holderith et al., 2012).

The strong immunoreactivity seen in the WT sections (Figs. 2-4, 8) was largely disappeared in the Ca$_v$2.3 KO sections (Fig. 4G). In order to quantitatively estimate the background labeling produced by the pan antibody, I counted the total number of immunogold particles observed in the 334 μm^2 area in the CA1 radiatum in both WT and Ca$_v$2.3 KO sections. I counted a total of 540 immunogold particles in WT and 15 in KO in the postsynaptic compartments (dendrites and spines) and 216 immunogold particles in WT and 51 in KO in the presynaptic compartments.

Ca$_v$2.3 channels are mostly postsynaptic in CA1 region

In the CA1 of the hippocampus, immunogold labeling was observed postsynaptically in the somata, dendritic shafts, and spines of the putative pyramidal cells (Figs. 3A-D, 4A, C-F). In the PSR, the big (Fig. 4E) and the small (Fig. 4A) caliber dendrites were both immunopositive for Ca$_v$2.3. In the presynaptic compartments, Ca$_v$2.3 labeling was detected at the extrasynaptic plasma membrane (Figs. 3C, E, 4B, D), and over the presynaptic AZ (Figs. 3A, D). Particles were seen in both inhibitory buotons terminating on pyramidal cell dendrites (Fig. 3C, 4B). In some cases, a presynaptic terminal and its postsynaptic spine were both seen to be positive for Ca$_v$2.3 (Figs. 3A, D, 4D). Plasma membranes of myelinated axons were also positive for Ca$_v$2.3 (Fig. 3F). In contrast to neuronal elements, glial cells showed no immunoreactivity for the protein.

The predominant postsynaptic localization of Ca$_v$2.3 subunit in the SO and PSR was clearly apparent from the qualitative analysis of the immunogold particle distribution. In order to provide a numerical comparison of the immunogold particles between the post- and presynaptic compartments, quantitative analysis was performed from 20 ~ 30 serial sections obtained from PSR (within 100 μm from the soma). Out of the 4122 plasma membrane bound particles counted, 3225 (78.2%) were observed in the postsynaptic (dendritic shafts and spines) and 897 (21.8%) in the presynaptic compartments. Postsynaptically, 1967 (47.7%) particles were observed in the dendritic shafts and 1258 (30.5%) in the spines. In the presynaptic compartment, 29 (0.7%) particles were observed in the AZ and 868 (21.1%) particles were seen in the rest of the

presynaptic plasma membrane. This quantitative data obtained from PSR further strengthens my qualitative observations regarding predominant postsynaptic localization of $Ca_v2.3$ in the CA1.

Quantification of the relative channel density between dendritic shafts, spine heads and somata

The subcellular distribution of ion channels at the neuronal plasma membrane can be highly regulated and complex. Ion channels can either be distributed uniformly or be selectively targeted to a specific neuronal compartment at a significantly higher density (see review, Nusser, 2009). To examine whether $Ca_v2.3$ shows uniform or compartmentalized distribution, dendritic spine heads, shafts, and somata of pyramidal cells were investigated in 15-30 serial ultrathin sections and the average immunogold particle densities in each of these domains were calculated (Fig. 5A). Completely reconstructed spines, whose heads could be clearly distinguished from their necks, were included in the analysis.

From a total of 19 dendritic shafts and 119 spine heads studied in the SO, the average immunogold particle density was 8.7 ± 0.52 particles/μm^2 (median = 8.2 particles/μm^2, range = 5.3 ~ 14.5 particles/μm^2) and 9.2 ± 0.65 particles/μm^2 (median = 8.2 particles/μm^2, range = 0 ~ 30.6 particles/μm^2), respectively ($P = 0.80$, Mann-Whitney U-test). In the PSR, 30 dendritic shafts and 154 spines were analyzed. The average immunogold particle density was 9.4 ± 0.49 particles/μm^2 (median = 9.0 particles/μm^2, range = 5.4 ~ 16.7 particles/μm^2) in the dendritic shafts and 8.6 ± 0.63 particles/μm^2 (median = 7.8 particles /μm^2, range = 0 ~ 40.4 particles/μm^2) in the spine heads ($P = 0.17$, Mann-Whitney U-test, Fig. 5A). When the average immunogold particle density was compared across the strata, no statistical difference could be revealed either between the dendrites ($P = 0.37$, Student's t-test) or between the spines ($P = 0.33$, Mann-Whitney U-test). Interestingly, much higher variability of $Ca_v2.3$ density was observed in spines than in the dendritic shafts [coefficient of variation (CV) in spines: SO, 0.78, PSR, 0.91. CV in dendrites: SO 0.26; PSR 0.29).

To obtain information about the abundance of RTCC in the pyramidal cell somata, the immunogold particle density was calculated from the partially reconstructed

pyramidal cell somata (n = 6). An average immunogold particle density of 5.3 ± 0.57 particles/μm^2 (median = 5. 7 particles/μm^2, range: 3.0-6.6 particles/μm^2) was obtained in this compartment, which was significantly lower than that of dendrites in SO and PSR (P < 0.01, one way ANOVA).

Immunogold density in primary apical dendrites and oblique dendrites

There is an increasing interest regarding the difference in ion channel density between the primary apical dendrites and their oblique branches. These two dendritic segments differ in their diameter and thus in the surface to volume ratio. In addition, the oblique dendrites harbor most of the spines and will therefore receive stronger excitatory inputs when compared with the primary apical dendrites (Megias et al., 2001; Frick et al., 2003). Thus, it would be informative to compare the expression density of calcium channels between these two dendritic compartments. However, partly because dendritic patch recordings are still inaccessible to the small oblique branches, data bearing on the issues of relative channel density and the possible differences in the signal processing mechanisms between primary apical dendrites and their oblique branches are largely lacking. Due to the technical advantage of EM methods in studying channel distribution, I was able to explore how $Ca_v2.3$ density compares between primary apical and oblique dendrites. When I measured the dendritic diameters of individual dendritic shafts in PSR, I found that the dendrites could be classified into two groups (Fig. 5B). One group had a dendritic diameter ranging from 0.58 to 1.12 μm (n = 7) and the other group had a dendritic diameter ranging from 0.21 to 0.36 μm (n = 23). These two groups putatively represent primary apical dendrites and oblique dendrites, respectively. The average labeling density in the primary apical dendrites was 8.3 ± 0.61 particles/μm^2 (median = 8.0 particles/μm^2, range: 6.6 ~ 11.5 particles/μm^2) and in oblique dendrite was 9.7 ± 0.61 particles/μm^2 (median = 9.5 particles/μm^2, range: 5.4 ~ 16.7 particles/μm^2). When the average labeling density was compared between these two dendritic populations, no significant difference could be detected (P = 0.25, Student's t-test), suggesting that oblique dendrites realize higher intracellular calcium rises than primary dendrites upon depolarization. It is also important to note that there was a larger variability in oblique than primary apical dendrites (CV, 0.30 and 0.19 for oblique and primary apical dendrites,

respectively) in the labeling density among individual dendrites. Such variability may suggest that each segment of oblique dendrites acts as a functional unit with distinct calcium dynamics and excitability.

Proportion of immunogold particles between spine head and spine neck

A previous two-photon calcium imaging study of Bloodgood and Sabatini (2007) has reported that $Ca_v2.3$ channels are localized in the spine heads, but not in the spine necks. However, spine necks are too small to be resolved well even by two-photon microscopy. Therefore, I examined whether or not $Ca_v2.3$ is selectively localized to spine heads. I found that in some spines immunogold particles were localized not only to the head, but also to the neck (Figs. 3A and 4C). When I quantitatively compared the proportion of immunogold particles in head and neck, I found that 413 (83.9%) particles were localized to the head and 79 (16.1%) to the neck of spines (n = 119) in the SO. The average number of immunogold particles in the spine head was 3.5 ± 0.31 (median = 2, range = 0 ~ 13), whereas in the spine neck it was 0.7 ± 0.10 (median = 0, range = 0 ~ 6). In the PSR, 592 immunogold particles were counted in the spines (n = 154), out of which 468 (79.0%) were localized to the head and 124 (21.0%) were localized to the neck. In the PSR, the average number of immunogold particles found in the spine head and spine neck was 3.0 ± 0.27 (median = 2, range = 0 ~ 16) and 0.8 ± 0.10 (median = 0, range = 0 ~ 6) respectively. When immunogold particles in the neck and head of dendritic spines were considered, it was found that individual spines contained 0 ~ 13 immunogold particles (mean = 4.13 ± 0.33; median = 3) in the SO and 0 ~ 16 (mean = 3.8 ± 0.29; median = 3) in the PSR. These results clearly demonstrate that the $Ca_v2.3$ channels were localized not only to the head, but also to the neck, of dendritic spines in the SO and PSR.

Number of calcium channels in relation to the size of spine head

Synaptic plasticity, occurring at the spine, is dependent on calcium influx through the RTCCs (Yasuda et al., 2003). The ultrastructural localization of these channels in various spine compartments would help to better understand the mechanism these channels play in shaping plasticity. In order to explore the relationship between the number of immunogold particles with the spine head surface area and the spine head

volume, a total of 119 spines in SO and 154 spines in PSR were examined in serial sections. The surface area and volume of the spines were measured and the total number of immunogold particles in each spine head was determined. The mean surface area of spine heads was 0.34 ± 0.017 μm^2 (median = 0.29 μm^2, range = $0.07 \sim 1.01$ μm^2, total measured area 40.43 μm^2) in the SO and 0.32 ± 0.018 μm^2 (median = 0.22 μm^2, range = $0.09 \sim 1.23$ μm^2, total measured area 48.98 μm^2) in the PSR. A positive correlation could be found when the number of immunogold particles were plotted against spine head surface area (SO: r = 0.72, $P < 0.01$; PSR: r = 0.69, $P < 0.01$; data not shown). The larger spines contained higher number of immunogold particles in their spine head, when compared with smaller, thin-type spines. Although the majority of spine heads were found to be immunopositive, about 17% of spine heads in SO and 25% of spine heads in PSR lacked immunogold particle for $Ca_v2.3$.

The average head volume of the spines was 0.019 ± 0.001 μm^3 (median = 0.015 μm^3, range = $0.003 \sim 0.064$ μm^3) in SO and 0.017 ± 0.001 μm^3 (median = 0.011 μm^3, range = $0.002 \sim 0.082$ μm^3) in PSR. The values of the spine head volumes measured in my study are in good agreement with previously reported data (Harris and Stevens, 1989; Sabatini and Svoboda, 2000; Grunditz et al., 2008; Nicholson and Geinisman, 2009). When the number of immunogold particles in an individual spine head was plotted against their volume, a linear positive correlation was found between these two parameters (SO: r = 0.69, $P < 0.01$, PSR: r = 0.67, $P < 0.01$, Fig. 6). The regression line had a slope of 183 immunogold/μm^3 in the SO and 163 immunogold/μm^3 in the PSR. Despite a positive correlation of the number of immunogold particles with the spine head surface area and spine head volume, there was a large variability in the number of particles even within the spines of similar volume (CVs of the particle density: SO, 0.78; PSR 0.91; Fig. 6).

In order to assess the detection sensitivity of the immunogold labeling for $Ca_v2.3$, I also analyzed the immunogold particles in postnatal day 20 rat spines (Figs. 3G, 6C), in which the number and density of RTCCs in spines were estimated by using calcium imaging (Sabatini and Svoboda, 2000). When the number of immunogold particles in individual spines was plotted against spine volume, a positive correlation was observed between the immunogold particle number and the spine head volume (r = 0.70). The

number of immunogold particles in individual spine heads ranged from 0-19 in my study and 1-20 in Sabatini and Svoboda's study. The slope of the regression line also compared well between the two studies (my study: 263 immunogolds/μm^3; Sabatini and Svoboda's study: 230 channels/μm^3, the latter slope value was calculated from the average density of open channels and the average open probability of RTCC as 0.52 reported in the study). Together, these data shows that the pre-embedding method has a high sensitivity and gives a reliable indication for the number of $Ca_v2.3$ channels.

Distance from the Postsynaptic density (PSD)

Immunogold particles were found to be localized in and around the PSD of both perforated and non-perforated synapses (Figs. 7A-C). To assess the relative distribution of immunogold particles found in the synaptic and non-synaptic sites of the PSR spine heads, the lateral distances along the spine head plasma membrane from the closest edge of the PSD to the center of immunogold particles were measured. The distance of particles (n = 581) from the edge of the PSD ranged from -53.2 to 989.4. When distances were allocated to 60 nm wide bins and expressed as relative frequency, it was found that the immunogold particles were broadly distributed in the spine head (Fig. 7D). Next, I categorized the immunogold particles as synaptic (< 0 nm), perisynaptic (0-60 nm) and extrasynaptic (> 60 nm) based on previously defined criteria (Lujan et al., 1997). Immunogold particles for $Ca_v2.3$ were the most abundant in the extrasynaptic sites (80.7%, 469 of 581), with some immunogold pools in the perisynaptic (16.0%, 93 of 581) and synaptic sites (3.3%, 19 of 581).

Relationship with parent dendrites

Accumulating evidences suggest that spines compartmentalize calcium and operate independently from their parent dendrites (for review, see Yuste et al., 2000). If spines are independent functional compartments, then the expression of calcium channels may be regulated intrinsically by the spines irrespective of the density in their parent dendrites. Therefore, it is of interest to know if multiple spines along a single dendritic segment will show any correlation in the labeling density with their parent dendrites. To examine this issue, the average immunogold particle density in the spines, whose parent

dendrite was traceable, was plotted against the density in their parent dendrites (Fig. 8). No significant correlation (SO, r = -0.19, P = 0.17, Spearman's rank order test; PSR, r = 0.19, P = 0.12, Spearman's rank order test) could be observed between these two parameters, thereby suggesting an independent expression mechanism of $Ca_v2.3$ between dendrites and their spines.

Discussion

My results provide a detailed anatomical characterization of the RTCC pore forming subunit $Ca_v2.3$ in distinct subcellular compartments of the mouse brain. The major findings are as follows:

1. RTCCs are expressed ubiquitously in the brain with higher levels in the hippocampus, interpeduncular nucleus, striatum, pallidum, cortex, amygdala, olfactory tubercle, accumbens than other regions.
2. RTCCs are expressed predominantly in presynaptic compartments in the interpeduncular nucleus but predominantly postsynaptic in other regions.
3. RTCCs found in dendritic shafts and spines showed a higher density compared to somata in CA1 of the hippocampus.
4. Individual spine heads contained 0 ~ 16 $Ca_v2.3$ particles in adult mouse and 0 ~ 19 $Ca_v2.3$ particles in postnatal day 20 rat. The latter is consistent with the range of the RTCC number reported previously (Sabatini and Svoboda, 2000).
5. The number of RTCCs in the spine is positively correlated to the spine head volume.
6. The number of RTCCs is highly variable among individual spines.
7. The average density of RTCCs in spine has no correlation to the density in the parent dendrite.

General LM distribution of Cav2.3

The regional distribution of the $Ca_v2.3$ protein described here is in excellent agreement with the previously described *in situ* hybridization patterns (Soong et al., 1993; Williams et al., 1994; Allen brain atlas, Lein et al., 2007). In general, strong immunoreactivity was detected in brain regions where R-type calcium channels have

been previously studied using electrophysiological methods (for review, see Weiergraber et al. 2006). However, in regions such as the calyx of Held the immunoreactivity was very weak (similar to background level) despite previous electrophysiology experiment (Wu et al., 1999) suggesting their presence. The strong immunoreactivity in the thalamus and the prominent somatic staining in various brain regions reported by Yokoyama et al. (1995) were also not observed in my study. The discrepancy between Wu's observations and mine may have arisen from other subunits forming the RTCC current in the calyx of Held. It is important to note that R-type current could still be recorded in neurons such as the cerebellar granule cells and the dorsal root ganglion cells of $Ca_v2.3$ KO mice (Wilson et al., 2000). The difference in the age of the experimental animals between my study and the electrophysiological studies may also account for the discrepancy. For example, in contrast to my study which focused in adult mouse Wu et al.'s study was done in 8-10 days old rats. Interestingly, Iwasaki et al. (2000) have described P/Q-, N- and R-type VGCC in the calyx terminal of P10 rats, but only P/Q- type in postnatal day 13. This further substantiates the developmental change as a cause of the discrepancy between two studies.

Detection sensitivity of the immunolabeling method

Immunogold labeling methods are generally thought to underestimate the total number of target molecules. The degree of underestimation may vary depending upon the target molecules and the immunogold localization technique used (see review, Masugi-Tokita and Shigemoto, 2007). In order to validate the immunolabeling efficiency, functional analysis of the target molecules must be compared with the number of immunoparticles detected. The number of $Ca_v2.3$ immunogolds counted in this study correlated well with the number of channels in individual spine heads estimated previously using optical fluctuation analysis (my study: range, 0-19, slope = 263 channels/μm^2; Sabatini and Svoboda's study (2000): range, 1- 20, slope = 230 channels/μm^2). However, I found some spines showing no immunoreactivity for $Ca_v2.3$. These negative spines may not have been reported by Sabatini and Svoboda as spines whose variance in fluorescence was not different from the dark noise were excluded from their analysis. As a result of the high detection sensitivity for $Ca_v2.3$ with the pre-

embedding immunogold labeling method, this study provides a reliable estimate for the *in situ* density of RTCC in the neuronal plasma membrane.

Ca$_v$2.3 in postsynaptic compartment

My study revealed heterogeneity in the number of RTCCs expressed among dendritic spines (Fig. 5A, C). The source for this heterogeneity may result from intrinsic properties of the given spine or differences in cell lineages from which the spine originates. It is unlikely that the cell lineage dictates differential expression because even the spines protruding from the same dendrite display large variability (Fig. 8). It is more probable that the individual spine characteristics such as age or plasticity contribute to differential expression of RTCCs in spines. Regardless of the source of variability, my results support the idea that spines are individual biochemical compartments operating autonomously from their parent dendrites (Yuste et al., 2000).

Matsuzaki et al. (2004) have demonstrated that only a subpopulation of the spines, specifically the thin type, are susceptible to induction of long-term potentiation (LTP). To date, the molecular mechanism governing this phenomenon still remains elusive. It has been previously shown that the activation of SK2 channels, which would dampen the membrane depolarization, require calcium entry through both NMDA receptors and RTCCs (Bloodgood and Sabatini, 2007). Previous immunohistochemical (Takumi et al., 1999) and functional (Noguchi et al., 2005) studies have suggested that all spines are equipped with NMDA receptors and the number of NMDA receptors does not correlate with the size of the synapses and with the spine volume. However my results showed that the number of RTCCs increases with the spine volume, and the subpopulation of thin-type spines lacked RTCCs. Although the functional relevance of my observation remains to be experimentally tested, I envisage that the spines lacking RTCCs are susceptible to potentiation because of the inability to activate SK2 channels. Some thin spines and all larger spines that contain high numbers of RTCCs are less likely to be potentiated because RTCC opening in these spines leads to SK channel activation, which in turn would dampen changes in the membrane potential.

NMDARs and VDCCs, in particular the R-type, are the major sources of calcium influx into hippocampal spines. It is interesting to note that these two differ in terms of

their ultrastructural localization in the spines, which suggests distinct role of these channels in the spines. NMDA receptors are strictly concentrated in the PSD (Takumi et al., 1999) while RTCCs are rather abundant at the extrasynaptic plasma membrane. However, the underestimation of the $Ca_v2.3$ labeling due to the limited access of antibodies to PSD in the preembedding method (see review, Masugi-Tokita and Shigemoto, 2007) cannot be excluded. The restriction of NMDARs to the PSD, i.e. in opposition to the AZ, is important for faithful activation of the receptors by glutamate released at the AZ. However, there exists no necessity for the RTCC to be restricted to the PSD because the membrane depolarization created by the voltage change, which is required for RTCC opening, rapidly propagates throughout the spine head plasma membrane. The differential localization between these two spine head calcium sources also argue for their unique access to downstream effectors. The observed distribution pattern of $Ca_v2.3$ would also be beneficial for the activation of SK channels as they are also known to be present throughout the spine heads (Lin et al., 2008).

$Ca_v2.3$ in presynaptic compartment

The strong immunoreactivity for $Ca_v2.3$ of the medial habenula (MHb) terminals in the IPN is an interesting finding and is in sharp contrast to its predominant postsynaptic localization in other brain regions. Postsynaptic RTCC have been suggested to play major role in regulation of synaptic plasticity and dendritic excitability but little information is available regarding the function of presynaptic R-type channels. Although no brain nuclei to date has been shown to have purely R-type channel-mediated neurotransmitter release, this unique expression pattern of R-type channels in IPN warrants future experiments to determine their role in vesicular release in this nucleus. Interestingly, no mRNA transcripts for P/Q and N-type channels could be detected in the medial habenula (Ludwig et al., 1997). Thus, MHb-IPN pathway opens the possibility to study the biophysical properties and the functional roles of R-type channels in isolation.

In the IPN, immunogold particles were mainly observed at the extrasynaptic plasma membrane and only occasionally over the presynaptic AZ, indicating a distinct distribution pattern in comparison to $Ca_v2.1$ (Kulik et al., 2004; Holderith et al., 2012). This may suggest that RTCCs may play specialized functional roles, in addition to

neurotransmitter release, in the presynaptic compartments. For example, activation of presynaptic BK channels in the IPN (Knaus et al., 1996) by $Ca_v2.3$ may function to modulate the action potential. In all regions examined where $Ca_v2.3$ was localized to the presynaptic compartment, $Ca_v2.3$ immunogold particles were mainly seen to be remote from the AZ, indicating that this is a common organizational scheme of this channel in the presynaptic compartment.

In conclusion, my study provides a novel understanding of the unique pre and postsynaptic localization of $Ca_v2.3$ subunit in the brain.

References

Augustine GJ, Santamaria F, Tanaka K (2003) Local calcium signaling in neurons. Neuron 40:331-346.

Baldi R, Varga C, Tamas G (2010) Differential distribution of KCC2 along the axo-somato-dendritic axis of hippocampal principal cells. Eur J Neurosci 32:1319-1325.

Bloodgood BL, Sabatini BL (2007) Nonlinear regulation of unitary synaptic signals by $CaV_{2.3}$ voltage-sensitive calcium channels located in dendritic spines. Neuron 53:249-260.

Bourne JN, Harris KM (2008) Balancing structure and function at hippocampal dendritic spines. Annu Rev Neurosci 31:47–67.

Day NC,Shaw PJ, McCormack AL, Craig PJ, Smith W, Beattie R,Williams TL, Ellis SB, Ince PG, Harpold MM, Lodge D, Volsen SG (1996) Distribution of α1A, α1B and α1E voltage-dependent calcium channel subunits in the human hippocampus and parahippocampal gyrus. Neuroscience 71:1013–1024.

Fiala JC (2005) Reconstruct: a free editor for serial section microscopy. J Microsc 218:52-61.

Frick A, Magee J, Koester HJ, Migliore M, Johnston D (2003) Normalization of Ca^{2+} signals by small oblique dendrites of CA1 pyramidal neurons. J Neurosci 23:3243–3250.

Gasparini S, Kasyanov AM, Pietrobon D, Voronin LL, Cherubini E (2001) Presynaptic R-type channels contribute to fast excitatory synaptic transmission in the rat hippocampus. J Neurosci 21:8715-8721.

Giessel AJ, Sabatini BL (2011) Boosting of Synaptic Potentials and Spine Ca Transients by the Peptide Toxin SNX-482 Requires Alpha-1E-Encoded Voltage-Gated Ca Channels. PLoS One 6:e20939.

Grunditz A, Holbro N, Tian L, Zuo Y, Oertner TG (2008) Spine neck plasticity controls postsynaptic calcium signals through electrical compartmentalization. J Neurosci 28:13457-13466.

Harris KM, Stevens JK (1989) Dendritic spines of CA 1 pyramidal cells in the rat hippocampus: serial electron microscopy with reference to their biophysical characteristics. J Neurosci 9:2982-2997.

Holderith N, Lorincz A, Katona G, Rózsa B, Kulik A, Watanabe M, Nusser Z (2012) Release probability of hippocampal glutamatergic terminals scales with the size of the active zone. Nat Neurosci doi: 10.1038/nn.3137.

Iwasaki S, Momiyama A, Uchitel OD, Takahashi T (2000) Developmental changes in calcium channel types mediating central synaptic transmission. J Neurosci 20:59–65.

Knaus HG, Schwarzer C, Koch RO, Eberhart A, Kaczorowski GJ, Glossmann H, Wunder F, Pongs O, Garcia ML, Sperk G (1996) Distribution of high-conductance $Ca2^+$-activated K^+ channels in rat brain: targeting to axons and nerve terminals. J Neurosci 16:955–963.

Kulik A, Nakadate K, Hagiwara A, Fukazawa Y, Lujan R, Saito H, Suzuki N, Futatsugi A, Mikoshiba K, Frotscher M, Shigemoto R (2004) Immunocytochemical localization of the α1A subunit of the P/Q-type calcium channel in the rat cerebellum. Eur J Neurosci 19: 2169–2178.

Lenn NJ (1976) Synapses in the interpeduncular nucleus: Electron microscopy of normal and habenula lesioned rats. J Comp Neurol 166: 73–100.

Lin MT, Luján R, Watanabe M, Adelman JP, Maylie J (2008) SK2 channel plasticity contributes to LTP at Schaffer collateral-CA1 synapses. Nat Neurosci 11:170–177.

Lorincz A, Notomi T, Tamas G, Shigemoto R, Nusser Z (2002) Polarized and compartment-dependent distribution of HCN1 in pyramidal cell dendrites. Nat Neurosci 5:1185-1193.

Ludwig A, Flockerzi V, Hofmann F (1997) Regional expression and cellular localization of the α1 and β subunit of high voltage-activated calcium channels in rat brain. J Neurosci 17:1339–1349.

Lujan R, Roberts JD, Shigemoto R, Ohishi H, Somogyi P (1997) Differential plasma membrane distribution of metabotropic glutamate receptors mGluR1 alpha, mGluR2 and mGluR5, relative to neurotransmitter release sites. J Chem Neuroanat 13:219-241.

Masugi-Tokita M, Shigemoto R (2007) High-resolution quantitative visualization of glutamate and GABA receptors at central synapses. Curr Opin Neurobiol 17:387-393.

Matsubara A, Laake JH, Davanger S, Usami SI, Ottersen OP (1996) Organization of AMPA receptor subunits at a glutamate synapse: a quantitative immunogold analysis of hair cell synapses in the rat organ of Corti. J Neurosci 16:4457–4467.

Matsuzaki M, Honkura N, Ellis-Davies GC, Kasai H (2004) Structural basis of long-term potentiation in single dendritic spines. Nature 429:761-766.

Megias M, Emri Z, Freund TF, Gulyas AI (2001) Total number and distribution of inhibitory and excitatory synapses on hippocampal CA1 pyramidal cells. Neuroscience 102:527-540.

Nicholson DA, Geinisman Y (2009) Axospinous synaptic subtype-specific differences in structure, size, ionotropic receptor expression, and connectivity in apical dendritic regions of rat hippocampal CA1 pyramidal neurons. J Comp Neurol 512:399-418.

Noguchi J, Matsuzaki M, Ellis-Davies GC, Kasai H (2005) Spine-neck geometry determines NMDA receptor-dependent Ca^{2+} signaling in dendrites. Neuron 46:609-22.

Nusser Z (2009) Variability in the subcellular distribution of ion channels increases neuronal diversity. Trends Neurosci 32: 267–274.

Parajuli LK, Fukazawa Y, Watanabe M, Shigemoto R (2010) Subcellular distribution of α1G subunit of T-type calcium channel in the mouse dorsal lateral geniculate nucleus. J Comp Neurol 518:4362-4374.

Pereverzev A, Mikhna M, Vajna R, Gissel C, Henry M, Weiergräber M, Hescheler J, Smyth N, Schneider T (2002) Disturbances in glucose-tolerance, insulin-release and stress-induced hyperglycemia upon disruption of the $Ca_v2.3$ (α1E) subunit of voltage-gated Ca^{2+} channels. Mol Endocrinol 16: 884-895.

Peters A, Palay S, Webster H (1991) The fine structure of the nervous system: neurons and their supporting cells. New York: Oxford University Press.

Sabatini BL, Svoboda K (2000) Analysis of calcium channels in single spines using optical fluctuation analysis. Nature 408:589-593.

Sabatini BL, Oertner TG, Svoboda K (2002) The life cycle of Ca^{2+} ions in dendritic spines. Neuron 33:439-452.

Saegusa H, Kurihara T, Zang S, Minowa O, Kazuno A, Han W, Matsuda Y, Yamanaka H, Osanai M, Noda T, Tanabe T (2000) Altered pain responses in mice lacking α1E subunit of the voltage dependent Ca^{2+} channel. Proc Natl Acad Sci USA 97:6132–6137.

Sochivko D, Pereverzev A, Smyth N, Gissel C, Schneider T, Beck H (2002) The $Ca_V2.3$ Ca^{2+} channel subunit contributes to R-type Ca^{2+} currents in murine hippocampal and neocortical neurones. J Physiol (Lond) 542:699-710.

Soong TW, Stea A, Hodson CD, Dubel SJ, Vincent SR, Snutch TP (1993) Structure and functional expression of a member of the low voltage-activated calcium channel family. Science 260:1133-36.

Svoboda K, Tank DW, Denk W (1996) Direct measurement of coupling between dendritic spines and shafts. Science 272: 716-719.

Takahashi H, Magee JC (2009) Pathway interactions and synaptic plasticity in the dendritic tuft regions of CA1 pyramidal neurons. Neuron 62:102-111.

Takumi Y, Ramírez-León V, Laake P, Rinvik E, Ottersen OP (1999) Different modes of expression of AMPA and NMDA receptors in hippocampal synapses. Nat Neurosci 2:618-24.

Tottene A, Volsen S, Pietrobon D (2000) $α_{1E}$ subunits form the pore of three cerebellar R- type calcium channels with different pharmacological and permeation properties. J Neurosci 20:171-178.

Trommald M, Jensen V, Andersen P (1995) Analysis of dendritic spines in rat CA1 pyramidal cells intracellularly filled with a fluorescent dye. J Comp Neurol 353:260–274.

Weiergraber M, Kamp MA, Radhakrishnan K, Hescheler J, Schneider T (2006) The $Ca_v2.3$ voltage-gated calcium channel in epileptogenesis--shedding new light on an enigmatic channel. Neurosci Biobehav Rev 30:1122-1144.

Williams ME, Marubio LM, Deal CR, Hans M, Brust PF, Philipson LH, Miller RJ, Johnson EC, Harpold MM, Ellis SB (1994) Structure and functional

characterization of neuronal α1E calcium channel subtypes. J Biol Chem 269:22347-22357.

Wilson SM, Toth PT, Oh SB, Gillard SE, Volsen S, Ren D, Philipson LH, Lee EC, Fletcher CF, Tessarollo L, Copeland NG, Jenkins NA, Miller RJ (2000) The status of voltage-dependent calcium channels in α1E knock-out mice. J Neurosci 20:8566-8571.

Wu LG, Westenbroek RE, Borst JGG, Catterall WA, Sakmann B (1999) Calcium channel types with distinct presynaptic localization couple differentially to transmitter release in single calyx-type synapses. J Neurosci 19:726-736.

Yasuda R, Sabatini BL, Svoboda K (2003) Plasticity of calcium channels in dendritic spines. Nat Neurosci 6:948-955.

Yokoyama CT, Westenbroek RE, Hell JW, Soong TW, Snutch TP, Catterall WA (1995) Biochemical properties and subcellular distribution of the neuronal class E calcium channel α_1 subunit. J Neurosci 15:6419-6432.

Yuste R, Majewska A, Holthoff, K (2000) From form to function: calcium compartmentation in dendritic spines. Nat Neurosci 3: 653-659.

Figure legends

Figure 1. Ubiquitous expression of Ca$_v$2.3 in the mouse brain

A, Preincubation of Ca$_v$2.3 pan-epitope antibody with the epitope 3 peptide abolished Ca$_v$2.3 immunoreactivity. Note that the pattern and immunostaining intensity were not changed in those sections stained by the pan-epitope antibody preincubated with antigenic peptides against epitopes 1, 2 or 4. B, Brain sections reacted by epitope 2 antibody displayed strong immunoreactivity in cortex, hippocampus, striatum, amygdala and interpeduncular nucleus. C, A high magnification image of hippocampus showing stronger immunoreactivity for Ca$_v$2.3, obtained by using epitope 2 antibody, in stratum oriens (so) and stratum radiatum (sr) than in stratum laconosum moleculare (slm) of the CA1 area. Note that the immunoreactivity in the CA3 area is weaker than the corresponding area of the CA1. In the dentate gyrus (DG), the molecular layer (ml) and the hilar region (hi) show moderate immunoreactivity. D, Western blot analysis of hippocampus and cortical lysates from WT and Ca$_v$2.3 KO mouse brains by using the pan-epitope and epitope 2 antibodies. The band at around 250 kDa (arrow, predicted molecular weight of Ca$_v$2.3) (Soong et al., 1993) was present only in the WT preparation, not in the KO. E, Light microscopic images of mouse brain sections stained with Ca$_v$2.3 pan-epitope antibody. Staining was observed throughout the rostro-caudal extent of the brain. Particularly strong immunoreactivity for Ca$_v$2.3 was seen in the superficial layer of the cortex, hippocampus, striatum, amygdala and the interpeduncular nucleus. Immunoreactivity seen in the WT (a-d) brain was not visible in Ca$_v$2.3 KO brain (e and f). F, Transmembrane topology of Ca$_v$2.3α subunit showing the location of the amino acid residues (red rectangle) recognized by epitope 2 and pan-epitope antibodies used in this study. am, amygdala; ct, cortex; hp, hippocampus; ht, hypothalamus; ip, interpeduncular nucleus; sn, substantia nigra; st, striatum, th, thalamus. Scale bars, 500 μm.

Figure 2. Distinct pre or postsynaptic localization patterns of Cav2.3 among the brain regions

A-C, Electron micrographs showing immunogolds for Ca$_v$2.3 in layer 2/3 of the somatosensory cortex (A), amygdala (B), striatum (C). Most of the immunogolds in these regions are observed in the dendrites (d) and spines (s). D-F, Immunogolds are localized

to the dendrites (d), throny excerence spines (ts) and mossy fibre buotons (mf) in the CA3 stratum lucidum. In the mossy fibre buotons immunogolds can be seen directly over the active zone (arrow in E) or at extrasynaptic plasma membrane remote from the active zone (arrows in F). G-K, Strong immunolabeling for $Ca_v2.3$ is observed in the presynaptic terminals in the interpeduncular nucleus. Crest synapses buotons (G-I) and *en passant* buotons (J, K) are both positive for $Ca_v2.3$. Arrows show the typical morphology of crest synapse. Images C-K are obtained by using epitope 2 antibody. a, axon terminal; d, dendrites; mf, mossy fibre boutons; s, spines; ts, throny excerence spines. Scale bars, 500 nm.

Figure 3. $Ca_v2.3$ proteins are localized to both pre and postsynaptic compartments in the stratum oriens (SO) of CA1

Ultrastructural localization of immunogold particles for $Ca_v2.3$ in SO were revealed by pre-embedding immunogold labeling method using pan-epitope antibody (A-F). Immunoparticles were observed along the plasma membrane of dendritic shafts (d), spine head (s), spine neck (n), and axon terminals (a). Immunogolds are more abundant in the postsynaptic site. Particles were seen in presynaptic compartments either over the active zone (A and D, arrowheads) or at the extrasynaptic plasma membrane of boutons remote from release sites (A, C and E, arrows). Myelinated axons (m) were also positive for $Ca_v2.3$ (F). G, Immunogold particles for $Ca_v2.3$ are seen predominantly in the postsynaptic compartments in SO of the postnatal day 20 rat. Arrows show presynaptic immunogold particles. Scale bars, 500 nm.

Figure 4. $Ca_v2.3$ proteins are localized to both pre and postsynaptic compartments in the proximal stratum radiatum (PSR) of CA1 area

Electron micrographs showing immunogolds for $Ca_v2.3$ in CA1 PSR using pan-epitope antibody. A-E, Immunogold particles are localized to the plasma membrane of dendritic shafts (d), spines (s), and axon terminals (a). Particles in the presynaptic compartments were seen in the excitatory (a in panel D) as well as the inhibitory (B) terminals. In the dendritic domains, immunogolds were seen both in the small calibre (d in panel A) as well as in big calibre (E) dendrite. C, Immunogold particles are localized in the plasma

membrane of the spine neck (arrows) as well as spine head. D, Variability in the number of immunogolds were observed even among the similarly sized dendritic spines. One spine (S1) is strongly labeled, whereas, other spines (S2 and S3), are moderately labeled or found to be immunonegative (S4 and S5). F, Somatic plasma membranes are also immunopositive for $Ca_v2.3$. G, An electron micrograph taken from $Ca_v2.3$ KO sections reacted with the pan-epitope antibody. No immunogold particle could be seen in the dendrites (d) and spines (s) in the $Ca_v2.3$ Ko sections. Although most of the presynaptic labeling disappeared in the KO sections, some axons and presynaptic boutons (b) still displayed 1-2 immunogold particles (arrows). Scale bars, 500 nm.

Figure 5. Somatodendritic compartmentalization of $Ca_v2.3$ in the CA1

A, The density of immunolabeling for $Ca_v2.3$ in various neuronal compartments is plotted in two ways; a dot plot of individual data points (left) and a box-and-whisker plot (right) demonstrating quartiles, median, maximum and minimum of the data. Mean density is indicated with a dot. Quantification of $Ca_v2.3$ immunoreactivity demonstrated a higher average density of the channel protein in dendritic shafts when compared with pyramidal cell somata (*, $P < 0.01$ against dendrites in SO and PSR, one-way ANOVA). Note that even within the same neuronal compartment, the immunogold density is highly variable. The variability is the highest in spines, moderate in dendrites and lowest in the cell somata. Ori de, stratum oriens dendrites; Ori sp, stratum oriens spines; PSR de, proximal stratum radiatum dendrites; PSR sp, proximal stratum radiatum spines; soma, somata of CA1 pyramidal cells. B, Cav2.3 density is plotted against the dendritic diameter of individual dendritic branches in the PSR. Dendrites can be separated in two different groups (putatively, oblique and primary apical dendrites) based on their dendritic diameter. Mean and SEM of the labeling densities for the two groups are indicated by closed squares and error bars, respectively. Although the immunogold density in individual dendrites were somewhat variable, no difference in the average immunogold density was detected between primary and oblique dendrites ($P = 0.25$; Student t-test). C, Representative 3D image of a dendritic shaft and 7 daughter spines reconstructed from 19 serial sections. Synaptic contacts are shown in red color. The green and pink dots represent the immunogolds in the spines and shaft, respectively. Immunogold particles at

the back side of the structures are not shown. The immunogolds are distributed throughout the dendritic plasma membrane. Although all seven spines emerge from the same dendrite, a high variability in the number of Ca$_v$2.3 particles can be seen among the spines: one spine is strongly immunopositive for Ca$_v$2.3, whereas two others remain immunonegative. Scale cube, 0.2 μm on a side.

Figure 6. Number of Ca$_v$2.3 immunoparticles found in individual dendritic spines is correlated with the size of spine head

The number of immunogolds for Ca$_v$2.3 in the spine head were plotted against the volume of individual spine heads. The number showed a positive correlation with the spine head volume (A: adult mouse SO, r = 0.69, n = 119, $P < 0.01$, Spearman's rank order test, B: adult mouse PSR, r = 0.67, n = 154, $P < 0.01$, Spearman's rank order test, C: Postnatal day 20 rat, r = 0.70, n = 84, $P < 0.01$ Spearman's rank order test). Note that there is variability in the number of immunogolds even among the similarly sized spines.

Figure 7. Ca$_v$2.3 channels are localized throughout the spine head plasma membrane

Electron micrographs showing immunoreactivity for Ca$_v$2.3 at synaptic, perisynaptic and extrasynaptic plasma membrane of dendritic spine head (s). Both in thin (A, SO, left and middle; PSR, right) and mushroom spines (B, SO; C, PSR), immunogolds are localized in the vicinity as well as remote from the edge of the PSD. D, Histogram showing the lateral distances of immunogolds for Ca$_v$2.3 (n = 581) measured from the nearest edge of the postsynaptic density. Each bin represents 60 nm. The nearest edge of the PSD is defined as zero. Immunogolds exhibit a broad distribution within the spine head. Scale bars = 100 nm.

Figure 8. Average immunogold density for Ca$_v$2.3 among spines is independent from the density in the parent dendritic shaft

Scatter plots show the labeling density for Ca$_v$2.3 in individual spines (open diamond) in SO (A, n = 56) and PSR (B, n = 66) as a function of the labeling density in their mother dendritic shafts (SO, n = 12; PSR, n = 13). In both regions, the labeling density for Ca$_v$2.3 varies among dendrites. Also, the average labeling density in the spines (closed

square) is not correlated with that in the mother dendrites (SO, r = -0.19, P = 0.17, Spearman's rank order test; PSR, r = 0.19, P = 0.12, Spearman's rank order test).

Table 1

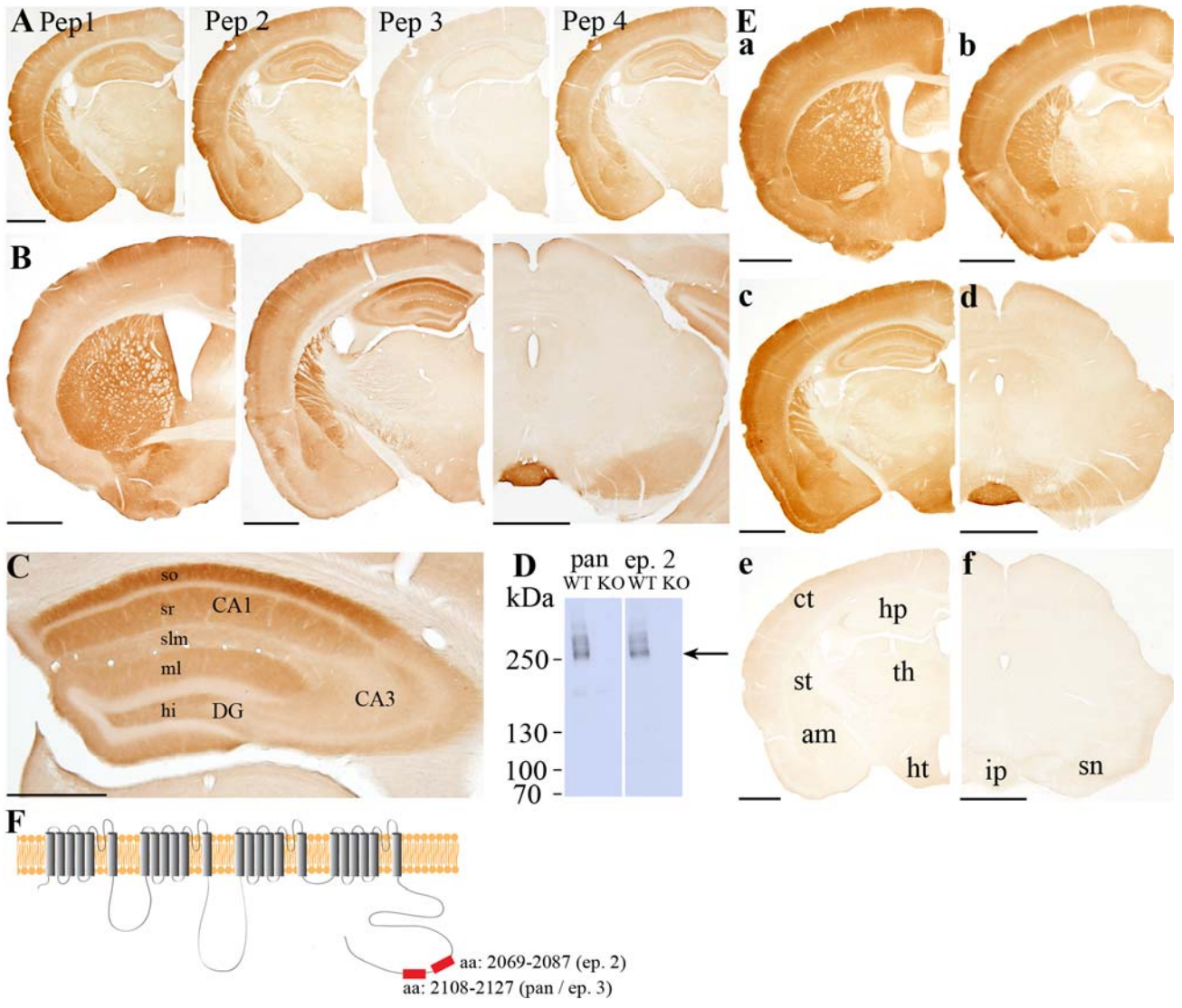Intensity of immunoreactivity for Ca$_v$2.3 subunit obtained with the epitope2 antibody

Area	Intensity in arbitrary unit	Category
Olfactory		
Main olfactory bulb	15 ± 0.6	low
Accessory olfactory bulb	13 ± 4.4	low
Anterior olfactory nucleus	18 ± 1.1	low
Olfactory tubercle	45 ± 6.3	high
Cerebral neocortex (somatosensory cortex)		
layer 1-3	45 ± 1.8	high
layer 4-6	20 ± 1.4	intermediate
Amygdala		
Central amygdaloid nucleus	44 ± 1.6	high
Lateral amygdaloid nucleus	20 ± 0.8	intermediate
Basolateral amygdaloid nucleus	36 ± 0.4	high
Basal ganglia		
Bed nucleus of stria terminalis	6± 0.9	low
Caudate putamen (striatum)	51 ± 3.2	very high
Accumbens nucleus (core)	43 ± 2.1	high
Accumbens nucleus (shell)	10 ± 0.2	low
Globus pallidus	48 ± 2.2	high
Substantia nigra	24 ± 1.5	intermediate
Ventral tegmental area -	-3 ± 0.8	negative
Subthalamic nucleus	3 ± 2.2	negative
Hippocampus		
CA1 Stratum laconosum molecularae	19 ± 1.2	low
Stratum radiatum	45 ± 0.8	high
Stratum pyramidale	N.A.	
Stratum oriens	65 ± 2.1	very high
CA3 Stratum lacunosum moleculare	16 ± 0.4	low
Stratum radiatum	8 ± 0.5	low
Stratum lucidum	14 ± 0.3	low
Stratum pyramidale	N.A.	
Stratum oriens	18 ± 0.8	low
Dentate gyrus		
Molecular layer	27 ± 0.1	intermediate
Granule cell layer	N.A.	
Hilus	24 ± 0.4	intermediate
Septum (Lateral)	24 ± 0.7	intermediate
Thalamus		
Lateral geniculate nucleus	-7 ± 0.7	negative
Medial Geniculate nucleus	13 ± 0.5	low
Reticular nucleus	-1 ± 0.7	negative
Epithalamus		
Medial Habenula	0 ± 1.2	negative
Lateral Habenula	-1 ± 1.1	negative
Hypothalamus	24 ± 0.1	intermediate

Reticular core		
Periaqueductal gray	-6 ± 0.8	negative
Ventral tegmental area	-3 ± 0.8	negative
Raphe nucleus	-10 ± 0.5	negative
Interpeduncular nucleus	60 ± 4.5	very high
Sensory brainstem area		
Cochlear nucleus	41 ± 0.6	high
Lateral superior olive	9 ± 0.5	low
Medial nucleus of trapezoid body	2± 0.1	negative
Superior colliculus	0 ± 1.0	negative
Inferior colliculus	4± 0.8	negative
Vestibular nucleus	2 ± 0.2	negative
Cerebellum		
Molecular layer	5 ± 0.7	low
Purkinje cell layer	N.A	
Granule cell layer	32 ± 0.6	intermediate
Pre-and postcerebellar nuclei		
Pontine nuclei	5 ± 0.6	low
Inferior olive	10 ± 3.7	low

Intensity of immunoreactivity for $Ca_v2.3$ was quantified in individual brain areas. Please see Materials and Methods for details of the quantification. Values are expressed as Mean ± SEM. Areas with significant immunosignals and related areas were shown in this table and those not listed were immunonegative for Cav2.3. Nuclei were grouped into 5 expression categories based on the intensity. Ranges of each categories are as follows; negative < 5; low 5 - < 20; intermediate 20 - < 35; high 35 - < 50; very high ≥ 50. N.A., not analyzed.

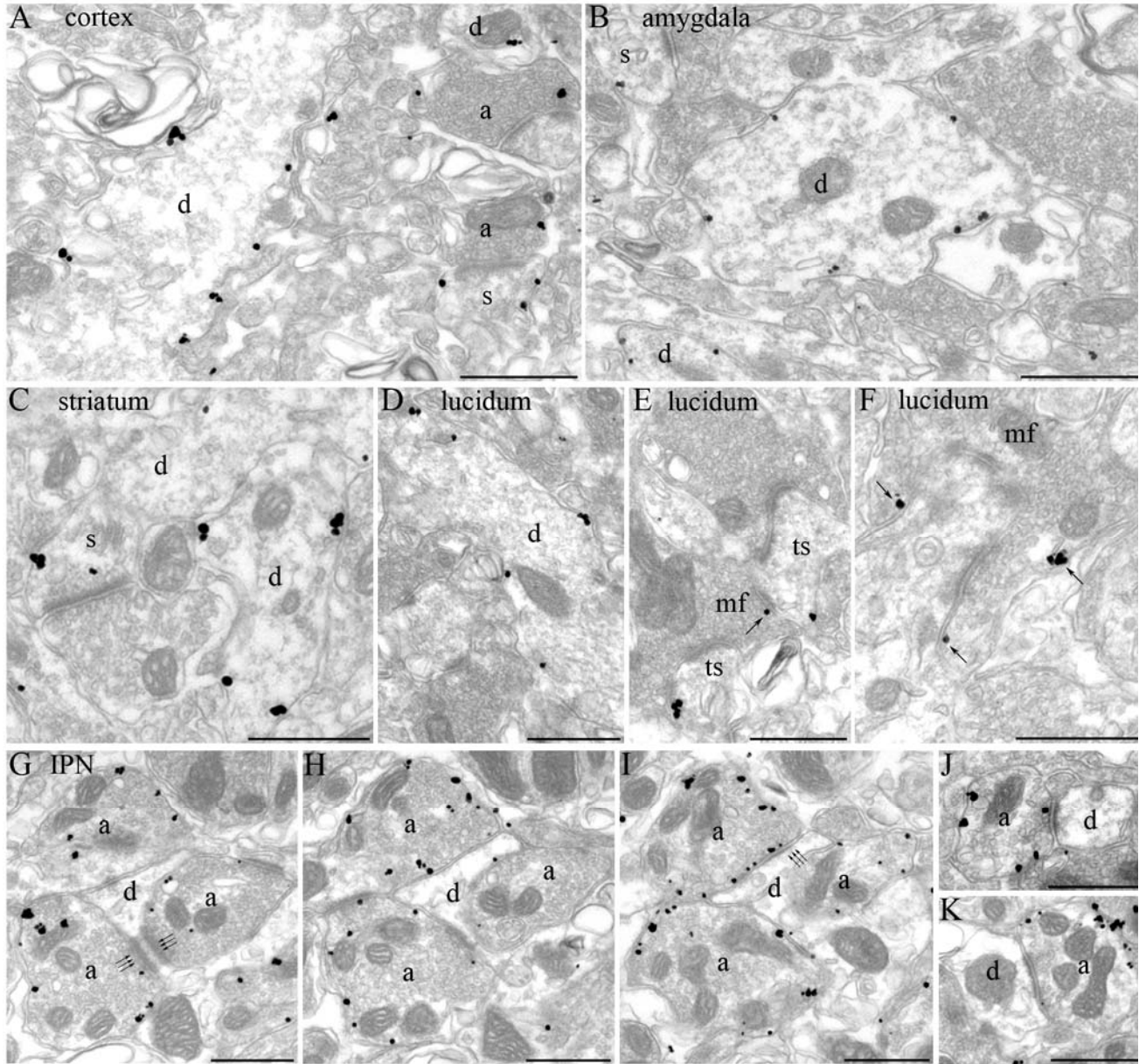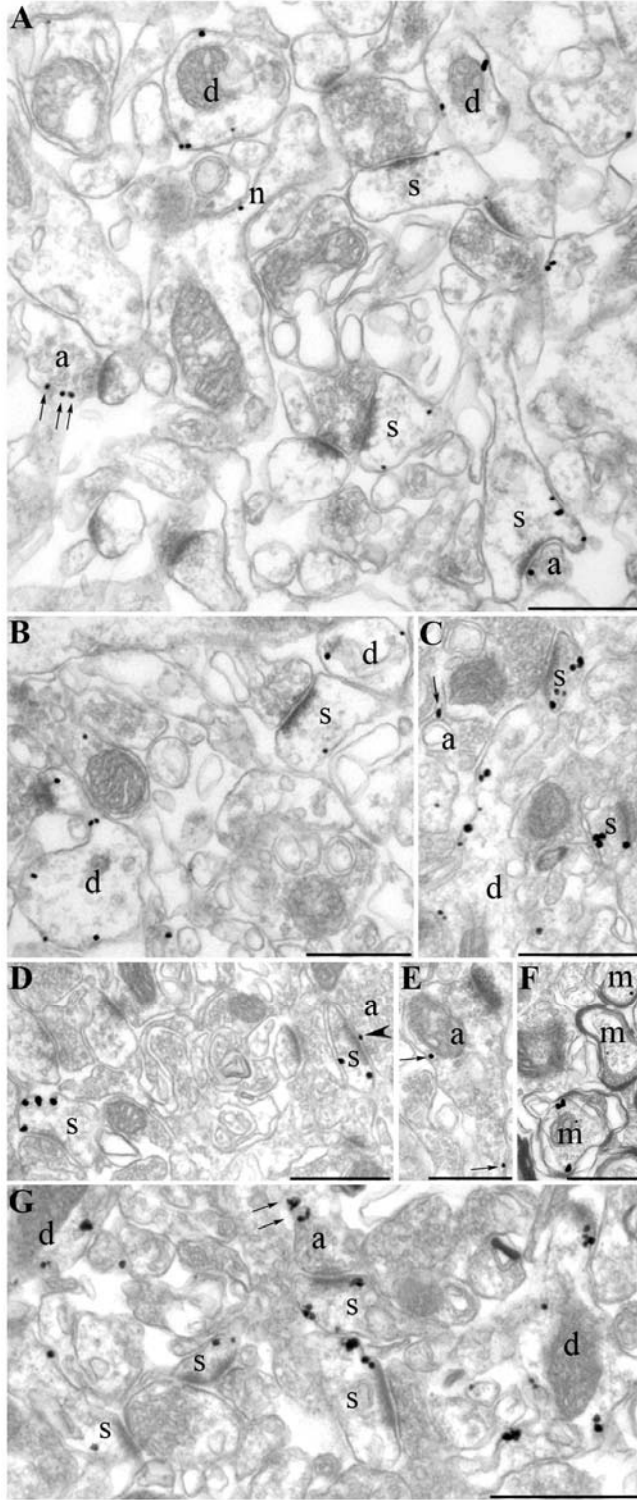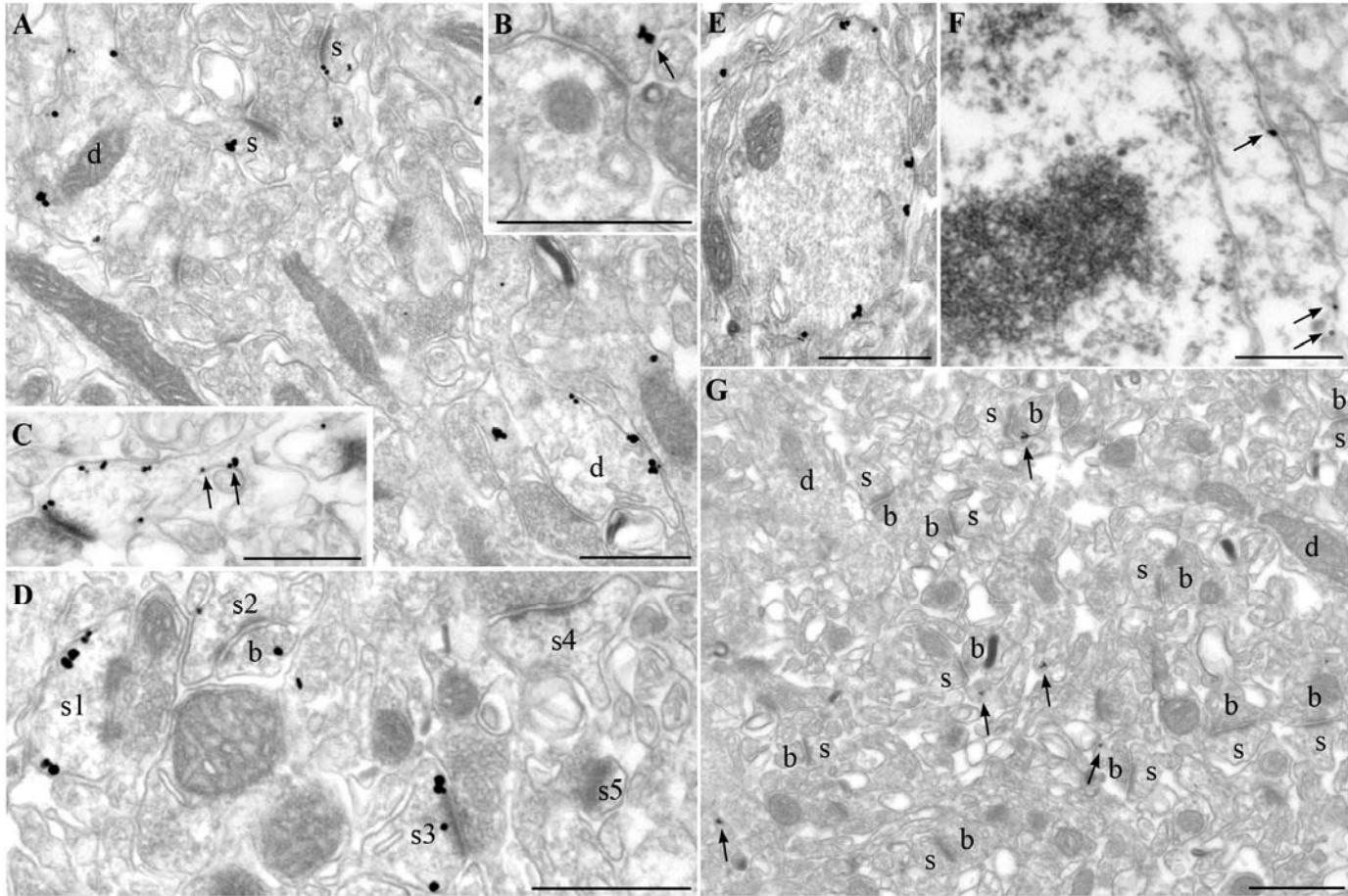**A** Pep1 Pep 2 Pep 3 Pep 4

B

C
so
sr   CA1
slm
ml
hi   DG   CA3

D
pan   ep. 2
kDa WT KO WT KO
250 -
130 -
100 -
70 -

E
a   b
c   d
e   f
ct   hp
st   th
am
ht   ip   sn

F
aa: 2069-2087 (ep. 2)
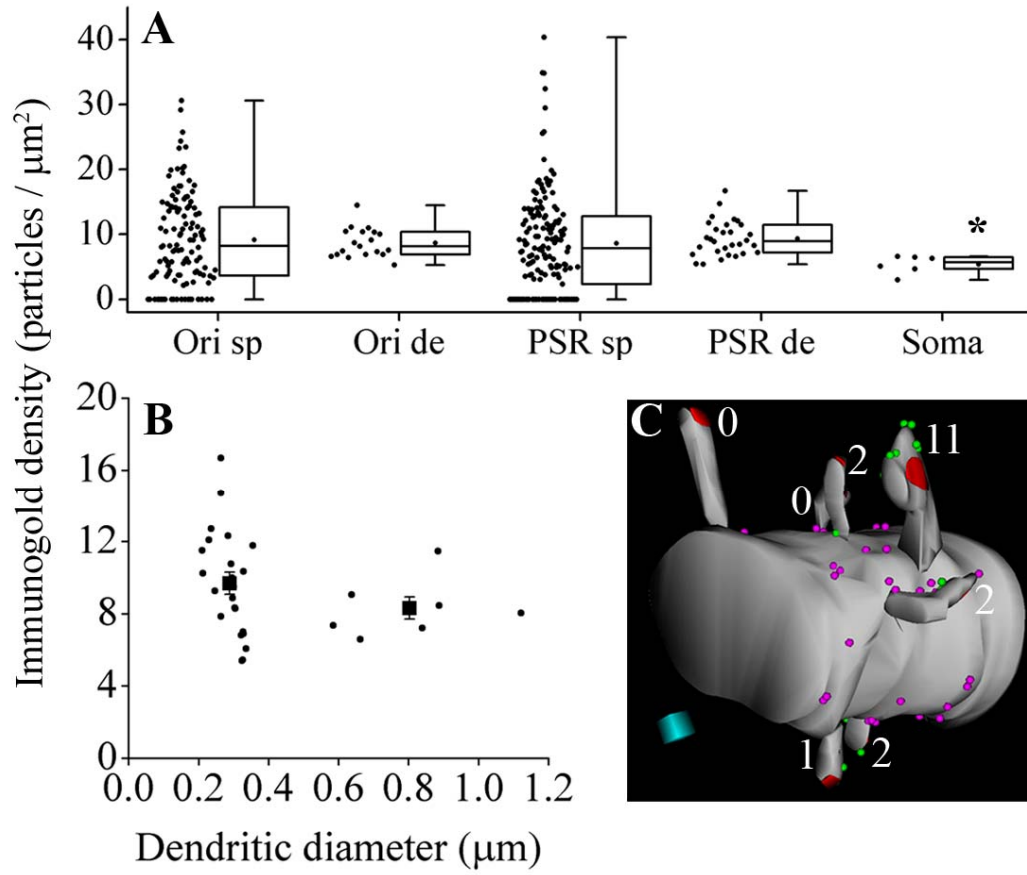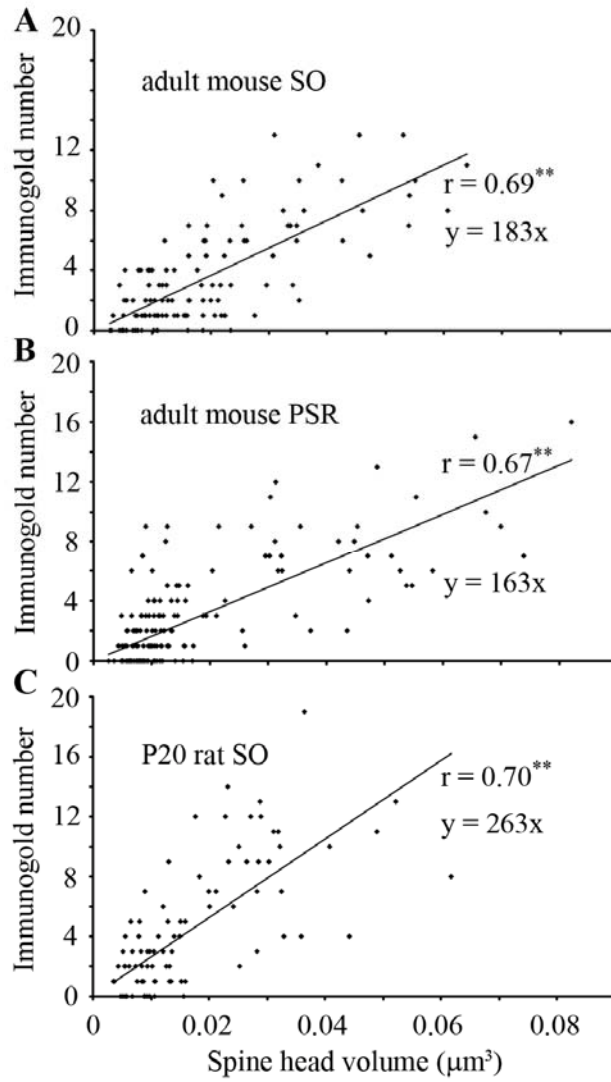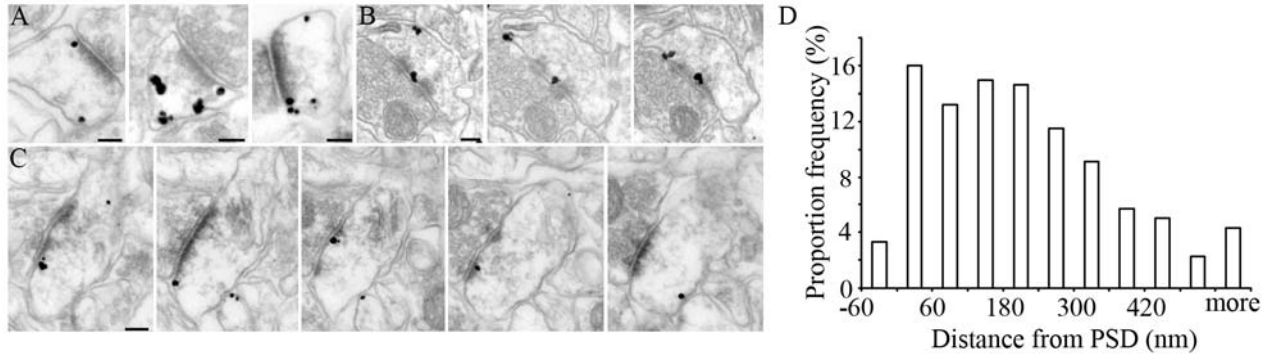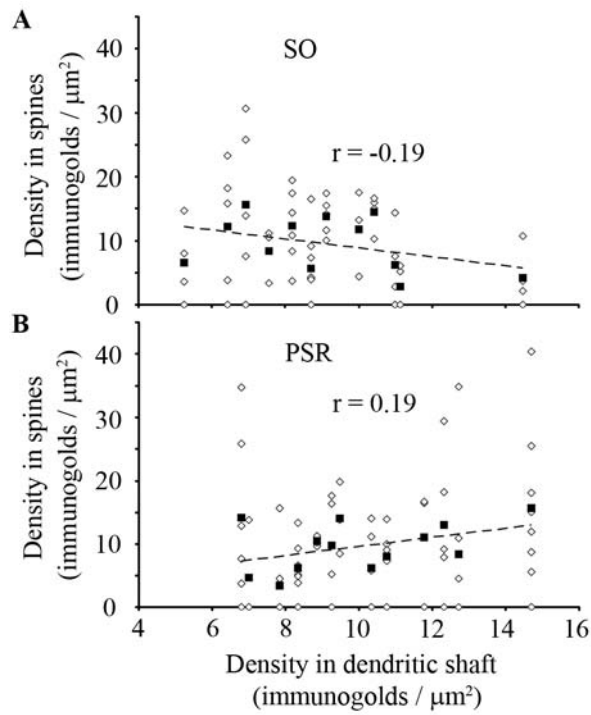aa: 2108-2127 (pan / ep. 3)

Figure 1

Figure 2

Figure 3

Figure 4

Figure 5

Figure 6

Figure 7

Figure 8